University of Nevada, Reno

Quantification of wildfire-induced perturbations to soil-water retention curves and their impact on rainfall runoff

A Thesis Submitted in Partial Fulfillment

of the Requirements for the Degree of Master of Science in Geology

by

Nathan R. Delgado

Dr. Scott W. McCoy/ Thesis advisor

May 2022

THE GRADUATE SCHOOL

We recommend that the thesis
prepared under our supervision by

NATHAN DELGADO

entitled

Quantification of Wildfire-Induced Perturbations to Soil-Water Retention Curves and Their Impact on Rainfall Runoff

be accepted in partial fulfillment of the
requirements for the degree of

MASTER OF SCIENCE

Scott W. McCoy, Ph.D
Advisor

Jason W. Kean, Ph.D
Committee Member

Ben W. Sullivan, Ph.D
Graduate School Representative

David W. Zeh, Ph.D., Dean
Graduate School

May, 2022

ABSTRACT

Increased frequency and magnitude of wildfires can cause elevated post-fire rainfall-runoff and debris-flow hazards in and around steeplands. Improved prediction of the severity and spatial extent of post-fire increases to these hazards requires understanding which soil properties are most strongly affected by wildfire and what role these changes play in runoff generation and debris-flow initiation. Previous studies have shown significant post-fire perturbations to saturated hydraulic conductivity (*Ks*) and sorptivity, and in some cases these perturbations appear to exert a strong control on the observed increase in post-fire runoff and debris flow. However, a variety of other soil properties also influence rainfall infiltration rates into unsaturated soils. The soil-water retention curve (SWRC), also called the soil-water characteristic curve, is the relationship between matric suction and soil-water content and determines many critical unsaturated soil properties such as unsaturated hydraulic conductivity. The SWRC is commonly described using the Van Genuchten equation, in which key parameters are the residual water content, θ_r, saturated water content, θ_S, the pore-size distribution index, *n*, and the inverse of the air-entry pressure head, α. To date, the degree to which SWRCs are perturbed by wildfire is less clear, and as a result, they are commonly assumed to be unaffected by wildfire and obtained based on soil texture from databases composed of unburned agricultural soils.

To quantify potential wildfire perturbations to SWRCs, we collected a suite of 43 unburned and 70 burned soil cores from seven recent wildfires in Nevada and California. We measured burned and unburned SWRCs and found best-fit Van Genuchten parameters θ_r, θ_s, n, α, using ASTM standard methods and the Meter HYPROP system. We found high quality fits to SWRCs from both unburned and burned samples using the Van Genuchten equation. While the magnitude of fire perturbation varies across fire sites, in most cases we found post-wildfire reductions in soil water retention at most values of matric suction, as quantified by increases in n and α, and decreases in θ_s and θ_r relative to the unburned state. To generalize the importance of the observed perturbations to SWRC parameters for rainfall runoff generation, we conducted a suite of numerical rainfall-runoff simulations in which we solved Richards equation with HYDRUS 1-D and with parameters constrained from burned and unburned SWRCs. These simulations suggest that the most commonly observed perturbations to SWRCs decrease time to ponding and strongly increase runoff generation at the sub-hourly timescales relevant to flash flooding and debris-flow initiation by rainfall runoff. These results highlight that field constraints on soil-hydraulic properties beyond just the saturated hydraulic conductivity are critical to more accurate prediction of rapid rainfall runoff following fire. The large database of such measurements presented here provides an important step towards increasing our understanding of the magnitude of expected post-fire perturbations to soil properties.

ACKNOWLEDGEMENTS

I would like to thank everyone that helped, supported, advised and encouraged me throughout my graduate school process. Thanks to my advisor, Scott McCoy, and my committee members, Jason Kean and Ben Sullivan. I would like to thank everyone else that contributed to this study and upcoming publication: David Cavagnaro, Scott McCoy, Matt Thomas, Don Lindsay, Ron Breitmeyer and Riley Cromie. A special thanks to David Cavagnaro for his help in the field and for his coding skills and plotting ideas that allowed us to visualize this large data set. We have spent countless hours on the road, many nights of camping, and grueling fieldwork days in everything from freezing temperatures and gale-force winds to 100+ degree days, to dense smoke. I would like to thank Matt Thomas for his modeling framework and help with the numerical simulations. Thanks to Riley Cromie and Ron Breitmeyer for training and advising me on the Meter HYPROP and WP4C systems.

I would like to thank the whole geomorph team for many great discussions, good times and support: Scott Feehan, Sophie Rothman, Joel Scheingross, Erika Groh, Conni DeMasi and Ingrid Suter. Lastly, I would like to thank my family (Mom, Dad, my sister Jessica, and my niece Kaya) and my partner, Alison Cramer, for constant love and support throughout this process.

Table of Contents

1.0: Introduction

Quantification of wildfire-induced perturbations to soil-water characteristic curves and their importance in generation of post-fire debris flows

Nathan Delgado[1], David Cavagnaro[1], Scott McCoy[1], Matthew A. Thomas[2], Donald Lindsay[3], Ronald Breitmeyer[4] & Riley Cromie[1]

1. Department of Geological Sciences and Engineering, University of Nevada, Reno, NV
2. USGS Geologic Hazards Science Center, Golden, CO
3. California Geological Survey, Redding, CA
4. Montana Bureau of Mines and Geology, Butte, MT

Manuscript for submission to the **American Geophysical Union Journal of Water Resources Research**

Sediment rich floods and debris flows are natural hazards faced by communities in and downslope of steep terrain. Debris flows, which are dense flows of rock, mud, and other debris (Iverson 1997) can be initiated by rainfall runoff during high-intensity rainstorms (McCoy et al, 2010, Kean et al., 2013) and become more likely following wildfires that burn at moderate to high severity (Staley et al., 2017). Debris flows are particularly hazardous following wildfire owing to rapid initiation times that requires no antecedent rainfall and that lag high intensity rainfall by as little as five to ten minutes (Kean et al., 2011) and owing to their large discharge that commonly exceeds that of a water flood at the same point in the channel by an order of magnitude (Kean et al., 2016).

Owing to a combination of factors, the geographical areas susceptible to post-fire debris-flow hazards are expanding. The frequency, size, and severity of wildfires as well as the length of the fire season is steadily increasing with warming climate and changing weather patterns (Westerling et al., 2006, Williams et al., 2019; Iglesias et al., 2022).

Population and infrastructure growth in foothill and mountainous areas that are prone to wildfires (Radeloff et al., 2018), alongside increased fire activity in areas that historically have not been affected by wildfires or debris flows has elevated the potential for loss of life and property resulting from post-fire debris flows (Cannon and DeGraff, 2009; Staley et al., 2017). The expansion of areas potentially exposed to post-fire debris-flow hazard has highlighted the need for robust post-wildfire debris-flow prediction (Cannon et al., 2008, 2010, 2011; Staley et al., 2013, Staley et al., 2017).

Debris-flow hazard can increase following wildfire due to the removal of vegetation and changes to the physical properties of soils that increase the efficiency of rainfall runoff and hillslope erosion, particularly in steep watersheds (Staley et al., 2014, McGuire et al., 2016). Overland flow and hillslope erosion can be increased following the destruction of canopy vegetation and surface leaf litter that protects soils from raindrop impacts and stabilizes hillslope sediments (McGuire et al., 2016). Destabilization of hillslope sediments can result in dry ravel loading of channels, which may increase the likelihood of post-fire debris flows (DiBiase and Lamb, 2020). Removal of vegetation can also reduce the hydraulic surface roughness of watersheds, further promoting overland flow (Rengers et al., 2019a, 2019b).

Post-fire perturbations to soil-hydraulic properties such as saturated hydraulic conductivity (*Ks*) and sorptivity may reduce the ability of water to infiltrate into soils which can increase runoff and subsequent debris-flow generation (Ebel, 2020a, Ebel 2020b, Ebel, 2012, Ebel et al., 2012 Ebel and Moody, 2020, Ebel and Moody, 2017, Moody et al., 2016, 2016b, Moody et al., 2009). Similarly, volatilized organic

compounds from burned vegetation can create a hydrophobic layer in the soil which prevents infiltration of rainfall and increases runoff (Moody et al., 2009, P. Pereira et al., 2018). While the perturbation to *Ks* and presence of a hydrophobic layer is starting to become better documented, the degree to which other properties of the soil critical to movement of water through the unsaturated zone, such as soil-water retention behavior and the unsaturated hydraulic conductivity, remain largely unconstrained.

The relative lack of constraints on potential post-fire changes to soil-water retention behavior, or the relationship between volumetric soil-water content and matric potential (i.e., the soil-water retention curve, SWRC) is particularly troubling because the SWRC in turn determines important properties of unsaturated soils ranging from the unsaturated hydraulic conductivity, soil strength, and plant available water. In unburned soils it is well-known that SWRCs depend sensitively on soil texture, soil structure, and organic matter content, all of which are soil properties known to be affected by fire (Certini, 2005; Mataix-Solera et al., 2011, Martínez et al., 2022).

Previous studies have suggested that wildfire effects on soil water-retention curves can be strongly influenced by organic matter and ash content and may be dominated by significant decreases in saturated soil-water content (Ebel, 2012, Ebel et al., 2012, Ebel and Moody, 2020a, 2020b). A 2012 study by Ebel included results of nine previous studies (Mallik et al., 1984, Boix-Fayos, 1997, Badia and Marti, 2003, Alauziz et al., 2004, Kitzberger et al., 2005, Gonzalez-Pelayo et al., 2006, Silva et al., 2006, Are et al., 2009, Stoof et al., 2009) of wildfire impacts on soil-water retention, soil particle-size distributions, organic water contents, permanent wilting point (i.e., the point at which

there is no water available to plants in the soil) and plant-available water (i.e., the difference between the field capacity of a soil and the permanent wilting point). In almost all cases there were post-fire decreases to organic matter content, the saturated water content, the water content at the permanent wilting point and overall soil-water retention. This study also reports an observed homogenization of post-fire soil-water retention and organic matter contents relative to differences observed in unburned soils. It is speculated that this is a result of the combustion and degradation of organic material and integration of ash into soil.

Furthermore, estimation of unsaturated soil properties using a single soil texture may not account for spatial heterogeneity in unsaturated storage and subsurface flow rates (Mirus and Loague, 2013, Mirus, 2015,) or post-fire perturbations to these properties. Due to the time-intensive nature and specialized equipment required to measure SWRC, these curves are commonly taken from agricultural databases of unburned soils (e.g., ROSETTA database, Schaap et al., 2001, Carsel and Parrish, 1988). This practice will miss any post-fire perturbations to soil-water retention behavior and potentially lead to mischaracterization of post-fire infiltration and runoff response to rainfall for a given soil texture.

To better understand potential post-fire perturbations to soil hydraulic properties beyond just the saturated hydraulic conductivity we seek to address three questions: 1) How are soil-water retention curves perturbed by fire? 2) How do post-fire perturbations to soil-water retention curves influence rainfall runoff and potential debris-flow generation? 3)

How do SWRC parameters for burned soils change with time after the fire? To address these questions, we collected a suite of 43 unburned and 70 burned soil cores from seven recent wildfires for laboratory analysis using ASTM standard methods, and the Meter HYPROP and WP4C systems to make measurements of changes to soil-water retention curves. These measurements were then used to characterize expected post-fire changes to runoff generation using a suite of numerical rainfall-runoff simulations in which we parameterized Richards equation with the laboratory measurements and then solved it with HYDRUS 1-D.

1.1: Fluid flow in unsaturated soils

A commonly used governing equation to describe the time rate of change of volumetric soil-water content θ (dimensionless) is Richards Equation (Richards, 1931)

$$\frac{\partial \theta}{\partial t} = \frac{\partial}{\partial z}\left[K(\psi)\left(\frac{\partial \psi}{\partial z} + 1\right)\right] \qquad \text{(Eq1)}$$

where *t* is the time, z is the vertical spatial coordinate (L, length), *K* is the hydraulic conductivity (LT^{-1}), and ψ is the matric potential or tension pressure head (L). Nonlinear functions that describe $K(\psi)$ are required to solve Equation 1, which owing to the difficulty of directly measuring $K(\psi)$ are commonly derived from the soil-water retention curve $\theta(\psi)$ using theoretical arguments to integrate across an increasing number of pathways of fluid transport, and hence increasing conductivity, as moisture content increases (e.g., Mualem 1976). One of the most widely used closed-form equations to describe soil water retention curves $\theta(\psi)$ is that proposed by Van Genuchten (1980)

$$\theta(\psi) = \theta_r + \frac{\theta_s - \theta_r}{(1 + |\alpha\psi|^n)^m} \qquad \text{(Eq2)}$$

which can be integrated using the theory proposed by and Mualem (1976), to describe how the unsaturated hydraulic conductivity changes as a function of θ or ψ

$$K(\psi) = Ks\left(\frac{\theta - \theta_r}{\theta_s - \theta_r}\right)^l \left[1 - \left(1 - \left(\frac{\theta - \theta_r}{\theta_s - \theta_r}\right)^{\frac{1}{m}}\right)^m\right]^2 \qquad \text{(Eq3)}$$

where θ_s is the volumetric soil-water content at saturation (dimensionless), θ_r is the residual soil-water content(dimensionless), α is the inverse of the air-entry ψ (L^{-1}), n is the pore-size distribution index (dimensionless), l is the pore-connectivity parameter (dimensionless) (l=0.5: Mualem, 1976), Ks is the saturated hydraulic conductivity (LT^{-1}), and $m = 1 - \left(\frac{1}{n}\right)$ (dimensionless).

Changes to soil properties alter the soil-water retention behavior and hydraulic conductivity of soils. One of the most widely observed controls on $\theta(\psi)$ are variations in soil texture owing to concomitant changes in distributions of pore sizes as grain size distributions change (Figure 1). For a nearly monodispersed clean sand, $\theta(\psi)$ approximates a step function as the tight distribution of pore sizes all drain at almost the same tension (Figure 2). In contrast to a clean sand would be a soil with much broader grain size distribution such as a loam or a till that releases water in a much smoother fashion owing to the wide range of pore sizes present (Figure 1).

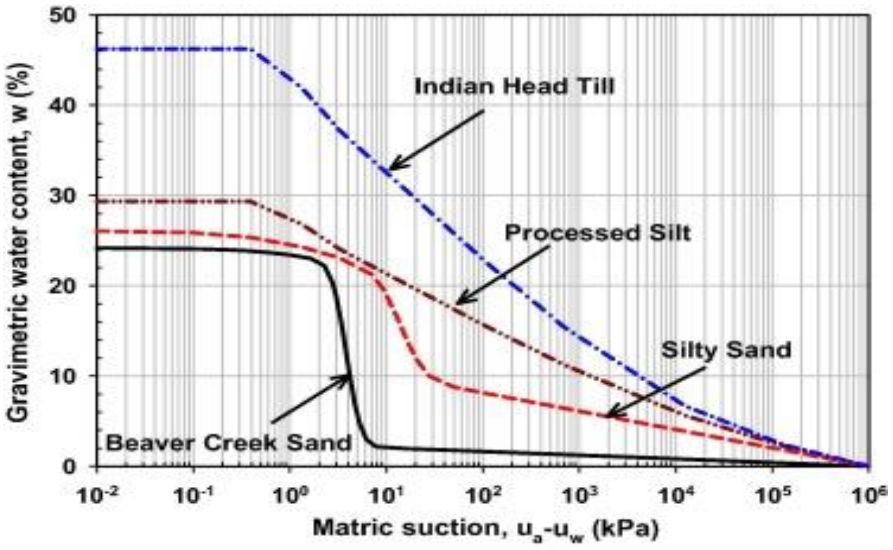

Figure 1. Example of typical soil water retention curves for different soil types from Fredlund et al., 2012.

To visualize effects of different parameter values when using the Van Genuchten soil-water retention and hydraulic conductivity curves, we iterate through a range of *n* and α values while holding all other parameters constant (Figure 2) and discuss below the impact of changing θ_s and θ_r. The parameters θ_s and θ_r determine the amount of water a soil can hold and thus can be thought of as storage terms that fix the left and right side of the soil-water retention curve (SWRC), respectively. Decreases in θ_s or increases in θ_r simply compress the SWRC along the Y axis. The parameter *n* is related to the pore size distribution and controls the rate of change of θ with ψ. As *n* increases, the SWRC steepens and becomes more step-like, such that the soil releases water over a narrower range of suction (Figure 2,A), and hence a well-sorted material such as sand has a high *n* value. Increased *n* also affects the hydraulic conductivity as a function of suction,

($K(\psi)$) and similarly steepens the $K(\psi)$ curve (Figure 2, B). For a saturated soil to begin to lose moisture the tension holding water in soil pores must be overcome by the air entry pressure, at which point water drainage can begin. The tension value at which drainage begins is called the air entry pressure. The parameter α is the inverse of the air entry pressure. Increases in α decrease the tension value at which the curve falls below saturation, which has the dominant effect of shifting both the $\theta(\psi)$ and $K(\psi)$curve to the left (Figure 2, C and D).

Understanding how changes to the Van Genuchten parameters influence the SWRC and $K(\psi)$ curves builds intuition as to the physical implications of potential post-fire perturbation to these curves, and how fire perturbations to these parameters relate to those commonly seen when shifting across different soil textures. There are several physical changes to soils that may result from exposure to wildfire. Combustion of organic matter and differences in cement type may cause soil structures to collapse, and volatilization of organic compounds can contribute to hydrophobicity in burned soils. Destruction of soil structure and decreased porosity due to ash-clogging may also lead to reduced infiltration and a hydrophobic layer, thus decreasing the water-storage capabilities of soils (Certini, 2005; Moody et al., 2015). The destruction of organic cements and introduction of ash can change the particle-size distribution (Giovannini and Lucchesi, 1997). Post-fire aggregation of fines can cause a coarsening of the particle-size distribution, leading to a distribution with a higher sand fraction (Ulery and Graham, 1993). Such changes in particle size should theoretically change the pore-size distribution index parameter, *n.*

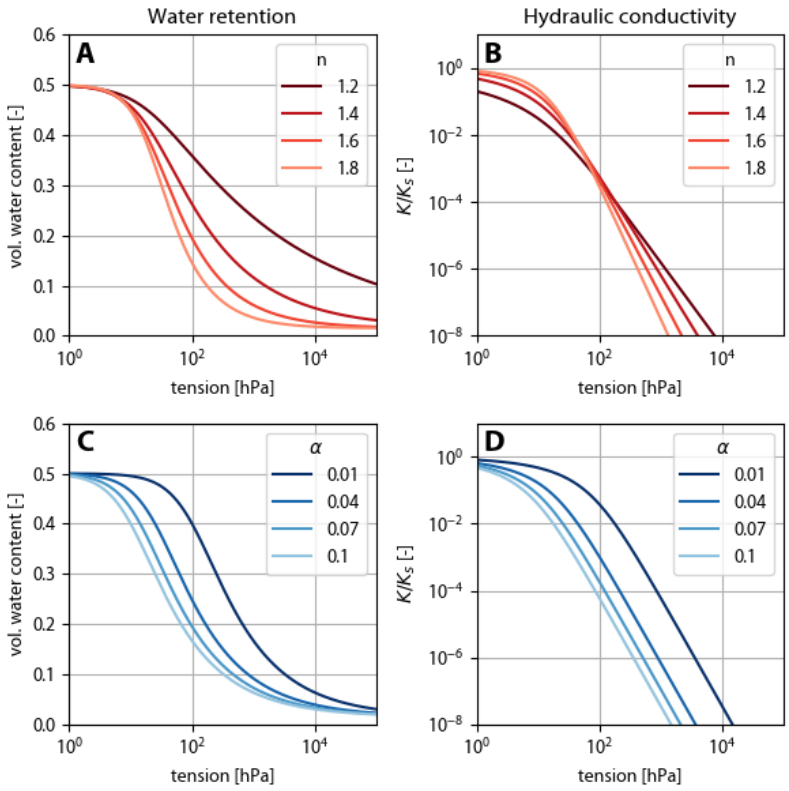

Figure 2. Changes in the shapes of soil-water retention curves $\theta(\psi)$ as represented by the Van Genuchten equation and related $K(\psi)$ curve that occur across a range of values for the pore size index n (**A**) and (**B**) and inverse air entry pressure α (**C**) and (**D**).

2.0: Study areas and field methods

We collected a suite of 43 unburned and 70 burned intact soil cores from seven recent wildfires in California (CA) and Nevada: the Carr fire in the northern CA Coast Ranges west of Redding CA, the Perry fire in the Nevada desert near Pyramid Lake, the Walker fire in the northern Sierra Nevada range near Genesee, CA, the Farad fire in the Sierra Nevada range near Truckee, CA, the Taboose fire on the eastern boundary of the Sierra Nevada range and Owens Valley near Fish Springs, CA, the Dixie fire, which burned in five CA counties in the northwest Sierra Nevada range, and the Dolan fire in the CA Coast Ranges near Big Sur, CA and to the east near Hunter Liggett, CA (Figure 3, Table

1). While these fires were selected opportunistically, the general selection criteria included landscapes that were steep and burned at medium to high soil burn severity such that the USGS post-fire emergency hazard assessment highlighted basins as having moderate to high likelihood for post-fire debris flows. Samples were collected from all slope aspects where possible. The resulting sample set can thus be considered as one made up of soils burned at moderate to high soil burn severity and unburned soils (here we refer to soils that had not burned in the last ten years as unburned) that developed in steep mountainous landscapes from varying bedrock lithology and climate.

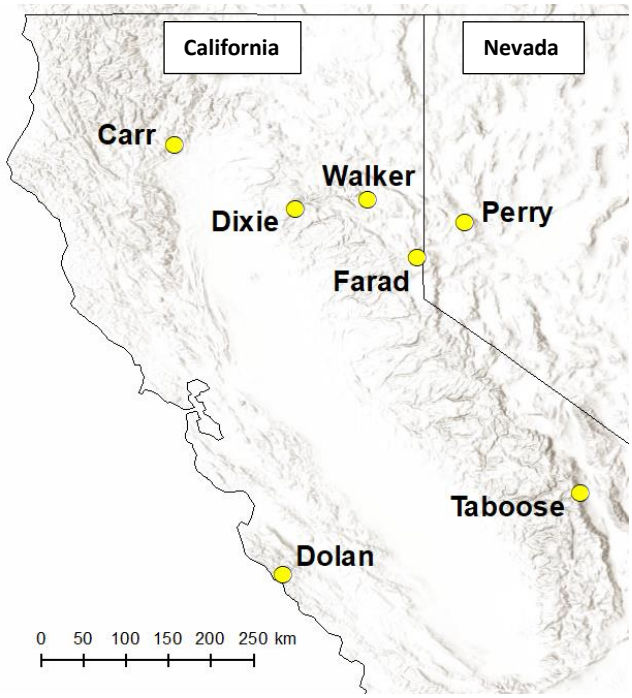

Figure 3. Map of studied fires.

Table 1. Summary of site-specific information for seven studied fires

Fire	Location	Burn Severity	Mean annual precipitation	1-year 15-minute rainfall intensity	Bedrock lithology	Vegetation Classification	slope angle	Time and name of last major fire at soil sample locations
Perry	Washoe County, NV	Moderate	310 mm/yr	19 mm/hr	Volcanic	Great Basin Shrub/Steppe	35-50	No recorded fires
Taboose	Inyo County, CA	Moderate	332 mm/yr	20 mm/hr	Granitic	Great Basin Shrub/Alpine Meadow	30-55	No recorded fires
Farad	Sierra County, CA	Moderate	530 mm/yr	23 mm/hr	Volcanic	California Mixed Conifer Forest	40-55	No recorded fires / Slight overlap with 2007 Highway fire at northern perimeter
Walker	Plumas County, CA	high	637 mm/yr	30 mm/hr	Granitic	California Mixed Conifer Forest, Ponderosa Shrub	35-55	2007 Antelope Complex
Carr	Shasta County. CA	high	1540 mm/yr	40 mm/hr	Granitic	California Mixed Conifer Forest, Ponderosa Shrub, California Chaparral, California Oakwoods	35-55	2008 Whiskeytown Complex
Dolan	Monterey County, CA	high	1300 mm/yr	40 mm/hr	Granitic, Metamorphic, Sedimentary	Redwood, California Chaparral, California Oakwoods, Coastal Sagebrush, Mixed Evergreen, California Grasslands	35-60	2008 Chalk fire, 2008 Indians fire, 2003 Carisso fire
Dixie	Butte County, CA, Plumas County, CA, Shasta County, CA, Tehama County, CA, Lassen County, CA	high	2570 mm/yr	44 mm/hr	Granitic, Metamorphic	California Mixed Conifer Forest, Ponderosa Shrub, California Chaparral, California Oakwoods	35-55	2012 Chips fire

2.1: Sample collection methods

To collect samples in an undisturbed state, we used a specimen ring insertion tool (Meter Group) specially designed for driving the stainless-steel specimen ring (Meter Group) into the soil. The insertion tool was connected to the smooth-edged top of the ring with the beveled cutting edge of the ring in contact with the soil and was hammered into the soil using a rubber mallet. Once the ring was fully embedded in the soil the insertion tool was removed. Using a flat-bladed masonry trowel, the soil around the ring was excavated and the ring was covered with a plastic cap. The soil was then further excavated until there was enough room to slide the trowel under the sample. The sample was lifted out of the soil

and flipped over, then the trowel was used to remove the excess soil and level the soil with the cutting edge of the specimen ring before installing another plastic cap (Figure 4). We took care to ensure to that the specimen ring was not underfilled to avoid overestimation of the saturated and residual water content during HYPROP analysis. Overfilling was always preferable as the excess can be removed in the lab during the sample preparation.

2.2: Packaging, Transport and Storage

The caps were secured with electrical tape and the sample was turned top-side-up before being labeled with the sample name and location. The sample was then wrapped with bubble wrap and stored top-side-up in a field pack until returning to the vehicle. Samples were then packed in a box and transported to the lab for storage. All samples were stored on a shelf in a climate-controlled room until later HYPROP and WP4C analysis.

2.3: Potential disturbance during transportation

Despite all efforts to maintain the undisturbed soil structure during sample collection and transportation, there are several factors that can lead to slight disturbances. Although the specimen rings have very thin walls and a sharp cutting edge, there is likely to be a small amount of soil-densification at the soil-specimen ring interface when the ring is driven into the soil. Occasionally rocks and/or woody debris are forced inward during this process and can disturb the in-situ soil structure. During field transportation the samples are carried in a backpack while hiking in steep and rough terrain. Additionally, the pack is repeatedly removed and placed on the ground throughout the day while collecting samples and other data. This makes it difficult to ensure that samples remain top-side-up

throughout the fieldwork campaign. The final issue is related to transportation in a vehicle. Many of our field sites required long and repeated drives on very rocky and uneven dirt roads and jeep trails, as well as long drives on mountain roads and highways. While these issues are unavoidable under some circumstances, we minimized disturbances to the soil, and associated errors during analysis, by strictly following identical sample collection, packaging, transportation and storage methods for all soil samples such that relative changes identified between burned and unburned soils should be robust.

Figure 4. Sample collection procedure. Photo from Shokrana and Ghane, 2020.

3.0: Lab Methods

We measured soil water retention behavior for the 43 unburned and 70 burned soil samples using the HYPROP apparatus and the WP4C dew point potentiometer (Meter Group, Pullman, WA) (ASTM 6836-02 Method D, ASTM International, 2016). The HYPROP (hydraulic property analyzer) measures the soil water retention curve (SWRC) using the simplified evaporation method (Fissel and Breitmeyer, 2017; Peters and

Durner, 2008). The HYPROP measures θ and Ψ during evaporative drying of an initially saturated soil sample. Upper and lower tensiometer shafts measure Ψ through pressure transducers in the sensor unit which measure suction with an accuracy of +/- 0.15 kPa. Throughout the evaporation process, mass of the sample is continually weighed on a high-precision balance (Figure 5). Combining the transient mass measurements with known initial conditions allows calculation of θ (Fissel and Breitmeyer, 2017, HYPROP manual, Meter Group, 2015). Using this technique, the water cavitation pressure is the highest tension value that can be measured.

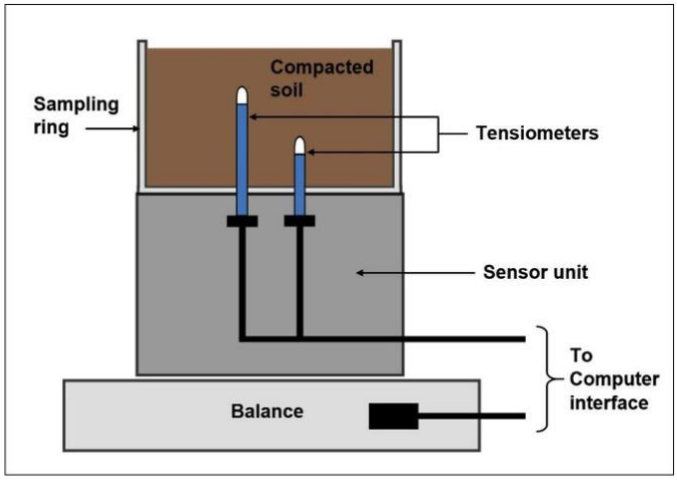

Figure 5. Meter HYPROP laboratory setup and schematic.

To measure tensions higher than the air entry point of the tensiometer we used the METER WP4C dew point potentiometer. The WP4C uses the relationship between relative humidity and soil-water potential to measure total suction in a dry soil (Fissel and Breitmeyer, 2017) and thus constrains the high suction-low water content portion of the SWRC that cannot be measured by the HYPROP. The WP4C uses a chilled mirror technique, which detects the condensation temperature on a mirror with a photoelectric

cell and uses the temperature reading to calculate the matric potential of the soil (Farrick et al., 2018).

Following the completion of each HYPROP experiment, the soil from the original specimen ring was placed in a 1-gallon storage bag for a minimum of 24 hours to allow the moisture to equilibrate, then three WP4C experiments were conducted using this material. This step in our methods deviates slightly from those recommended in the Meter Group HYPROP and WP4C manuals. The suggested method involves taking a sub-sample from the top, middle and bottom of the larger sample when decoupling the specimen ring from the HYPROP sensor unit, then covering those samples for a minimum of 24 hours to allow the moisture to equilibrate. In most cases, our soil samples lacked the cohesion to remain intact during the decoupling process, thus making the 3-layered sampling method difficult and hence we chose a method that could be uniformly carried out across all samples. Specimens for testing in the WP4C were prepared in 37 mm-diameter stainless steel specimen cups having a volume of 5.38 ml. The mass of soil required for each sample was determined by multiplying the bulk density of the soil from the HYPROP experiment with the volume of the WP4C specimen cups. A specially machined tamper was used to ensure that all specimens were compacted to a thickness of 5.0 mm. The three completed WP4C samples and the remaining soil from the HYPROP sample were oven-dried at 105°C for a minimum of 24 hours to get the final dry weight of the specimens. The volumetric water content and matric potential of each WP4C sample were used as additional data points for obtaining the final SWRC during the fitting process (Breitmeyer and Fissel, 2017, Meter Group) (Figure 6).

We estimated parameters for the Van Genuchten (1980) SWRC curve and resulting $K(\psi)$ curve Mualem (1976) (Equations 2 and 3) from the measured SWRC data using non-linear regression implemented in the proprietary HYPROP-FIT software package (Felling et al., 2019, Meter Group) as well as using the Python library scipy.optimize.curve_fit. We found both curve fitting packages fit equally well based on the root mean squared error and distributions of fit parameters across both methods were not shown to come from statistically different populations. Here we report the values obtained using HYPROP-FIT. Additionally, we compiled root mean squared error metrics of best fit Van Genuchten equations for both burned and unburned sample sets. If the saturated water content was allowed to be a fitted parameter, we found that the HYPROP-FIT software systematically overestimated the saturated water content of the sample. To correct for overestimation, we fixed the saturated water content to that calculated by taking the difference between the saturated and oven-dried weight of the sample, normalized by the volume of the sample. There were four cases in which the core barrels were underfilled by ~3-5 mm. The HYPROP-FIT software allows for a volume correction during the fitting process. In these cases, the missing soil volume was calculated and the necessary adjustments were made.

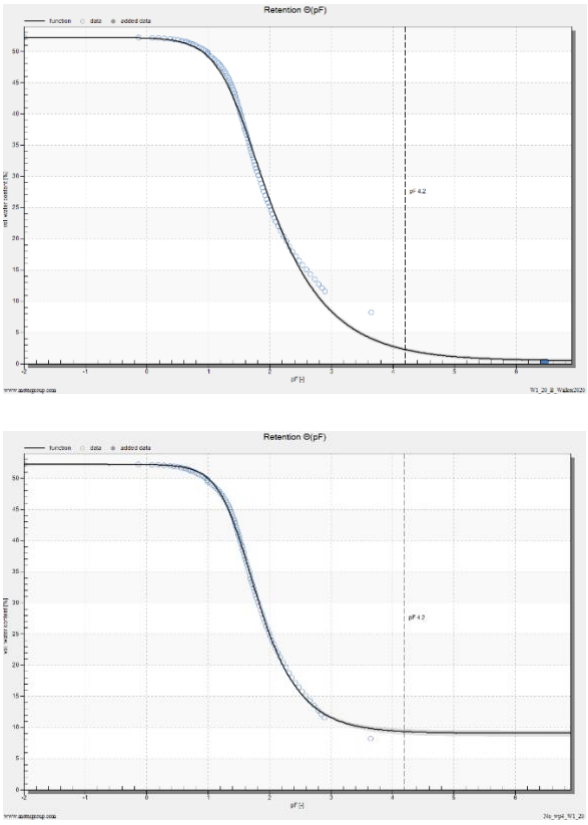

Figure 6. SWRC with added WP4C data (top) and with only HYPROP data (bottom).

3.1: Soil-water retention results

To determine if the Van Genuchten equation suitably describes SWRCs for both burned and unburned samples, we compiled the resulting root mean squared error (RMSE) as a goodness of fit metric for each population of samples. To facilitate comparison of RMSE across SWRCs with different scales we normalized RMSE by the range of water contents for each SWRC. Normalized RMSE data show that the Van Genuchten function fits data from unburned and burned soils equally well, with distribution means and standard deviation for unburned and burned being 2.3+/-1.0%, and 2.9+/-1.9%, respectively. According to a t-test these two populations do not come from different distributions at a

confidence of 90% (Figure 7). Despite similarity in distribution means between unburned and burned populations, the upper tail of the burned distribution does extend slightly beyond that of the unburned population. Burned samples with these poorer fits each have somewhat unique SWRCs that cannot be approximated by a single simple sigmoid; however, it is unclear if these curves resulted from poor connection between the tensiometer and the soil or from actual changes to retention behavior from burning. The burned population is also twice as large as the unburned population such that if both were of similar size a few samples with larger error might have been realized in the unburned population. Owing to the minor influence of these few samples with larger error on the overall burned error distribution, we conclude that the Van Genuchten equation suitably describes SWRCs for both burned and unburned samples.

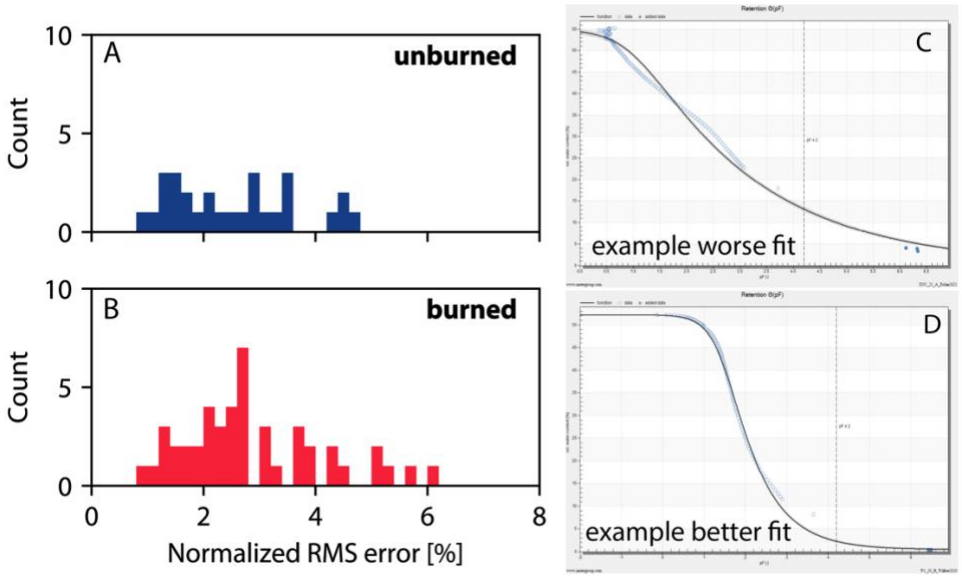

Figure 7. Histograms of normalized root mean squared error resulting from best fit Van Genuchten equations to the population of unburned samples (**A**) and burned samples (**B**). Examples of SWRCs from the high-end of normalized error (**C**) compared to a better fit example (**D**).

Owing to variability in parent lithology, landcover class, and climatology between wildfire sites we first look at resulting SWRCs and fire perturbations to those curves first grouped by wildfire location and then present results of the entire sample set grouped by burned versus unburned state, then grouped by time since burn, and finally by soil texture.

The perturbation resulting from burning soils at moderate to high soil burn severity is variable across all seven independent wildfire sites (Figure 8, Figure S1, Table S1 and S3). However, we do observe a post-fire reduction in soil-water retention at all fire sites, either across the entire range of matric potential (Taboose and Carr fire), or predominantly at low (Walker fire) or high values of matric potential (Perry fire). These post-fire reductions in soil-water retention lead to SWRCs that characteristically steepen while shifting down and to the left (such that soils release water over lower, and a narrower range of suction values). These changes in shape of position of SWRC curves result in increases in n and α and decreases to θ_r and θ_s across the majority of fires when compared to unburned samples from each fire location (Figure 9).

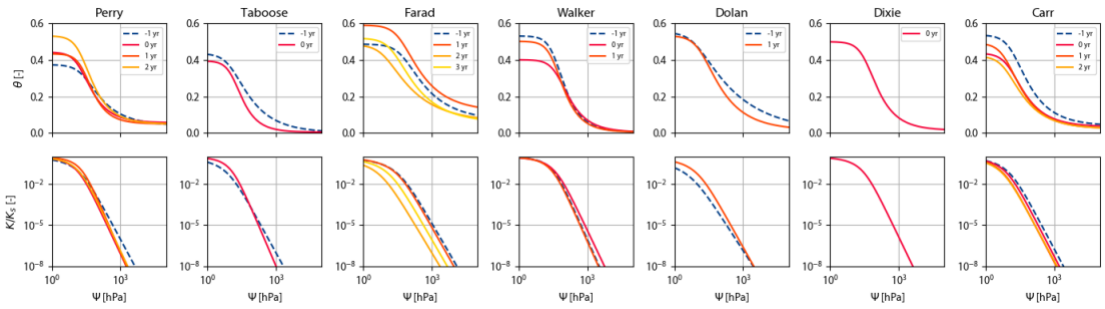

Figure 8. Soil-water retention curves for each fire site (top row) at various times postburn and corresponding normalized hydraulic conductivity curves (bottom row). Colors denote curves resulting from the mean parameters in each time-since-burning category, with the dashed blue line representing the mean of unburned samples at that site. Time step denoted by -1 refers to unburned samples.

Because the general direction of perturbation to SWRCs was generally consistent across all fire sites we present results obtained by grouping all fires into a single data set where trends might be considered characteristic for the region of California and Nevada sampled by our seven fire sites. When the entire data set is split into unburned vs burned data, we see considerable variability within each parameter distribution but the characteristic post-fire reduction in soil-water retention is clearly seen when comparing the mean burned and unburned SWRCs (Figure 12, E). This characteristic reduction in soil water retention is similarly achieved by post-fire increases in the rate of change terms, α and n, and a decrease in the storage terms, θ_r and θ_s. The mean burned SWRC shifts to the left and steepens such that burned soils across our fire sites are expected to release their water content over a narrower range of suction and generally have lower hydraulic conductivity at a given tension value (Figure 8).

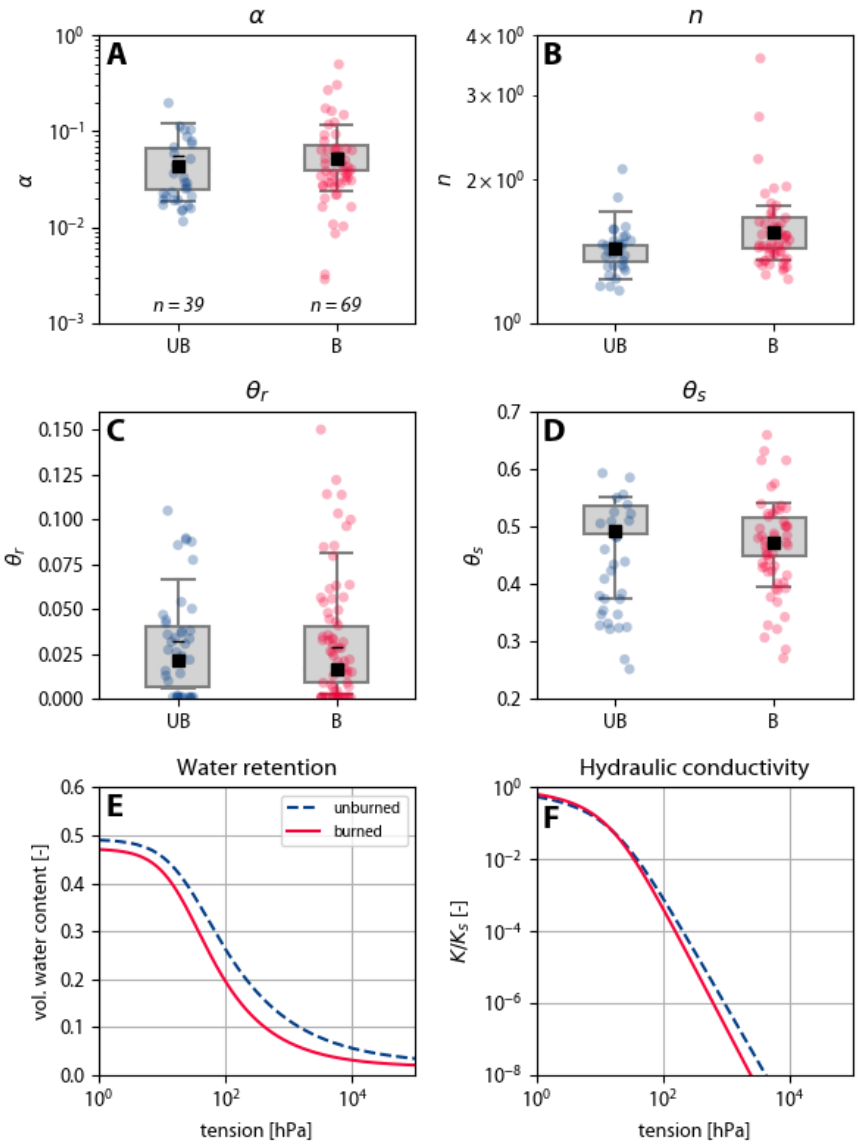

Figure 8. Compilation of best-fit Van Genuchten parameters showing distributions of inverse air entry pressure α (**A**), pore-size index n (**B**), residual soil-water content θ_r (**C**), and saturated soil-water content θ_s, (**D**) grouped by burned versus unburned samples. Blue points are for unburned samples, while red show burned samples. Boxes span the interquartile range, whiskers span the range of the data excluding outliers, black squares mark the geometric mean, small dash marks arithmetic mean. The corresponding mean soil-water retention curves for burned and unburned are shown in (**E**) and mean normalized hydraulic conductivity curves in (**F**). Colors correspond to burned versus unburned with dashed line showing the mean unburned curve and solid lines showing mean burned curves.

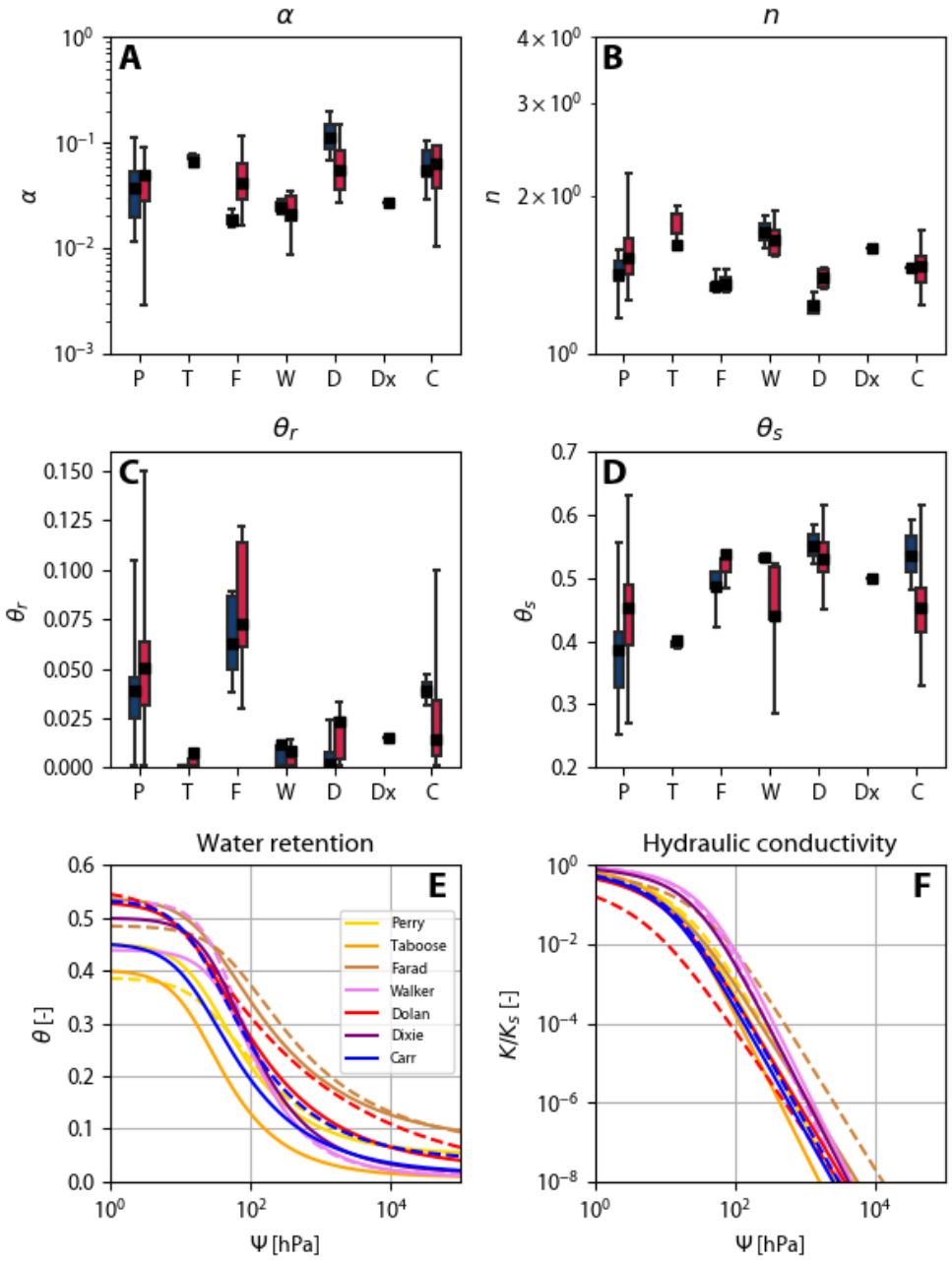

Figure 9. Compilation of best-fit Van Genuchten parameters showing distributions of inverse air entry pressure α (**A**), pore-size index n (**B**), residual soil-water content θ_r (**C**), and saturated soil-water content θ_S, (**D**) grouped by fire site. Blue box and whisker plots are for unburned samples, while red show all burned samples. Boxes span the interquartile range, whiskers span the range of the data, black squares mark the geometric mean. The corresponding mean soil-water retention curves for each fire site are shown in (**E**) and mean normalized hydraulic conductivity curves in (**F**). Colors correspond to fire site with dashed lines showing the mean unburned curves and solid lines showing mean burned curves.

When the entire data set is grouped by time, sublte trends of post-fire recovery can be identified across all Van Genuchten parameters except α. Parameters generally return towards unburned values within the three-year time span investigated for most fire sites (Figure 10).

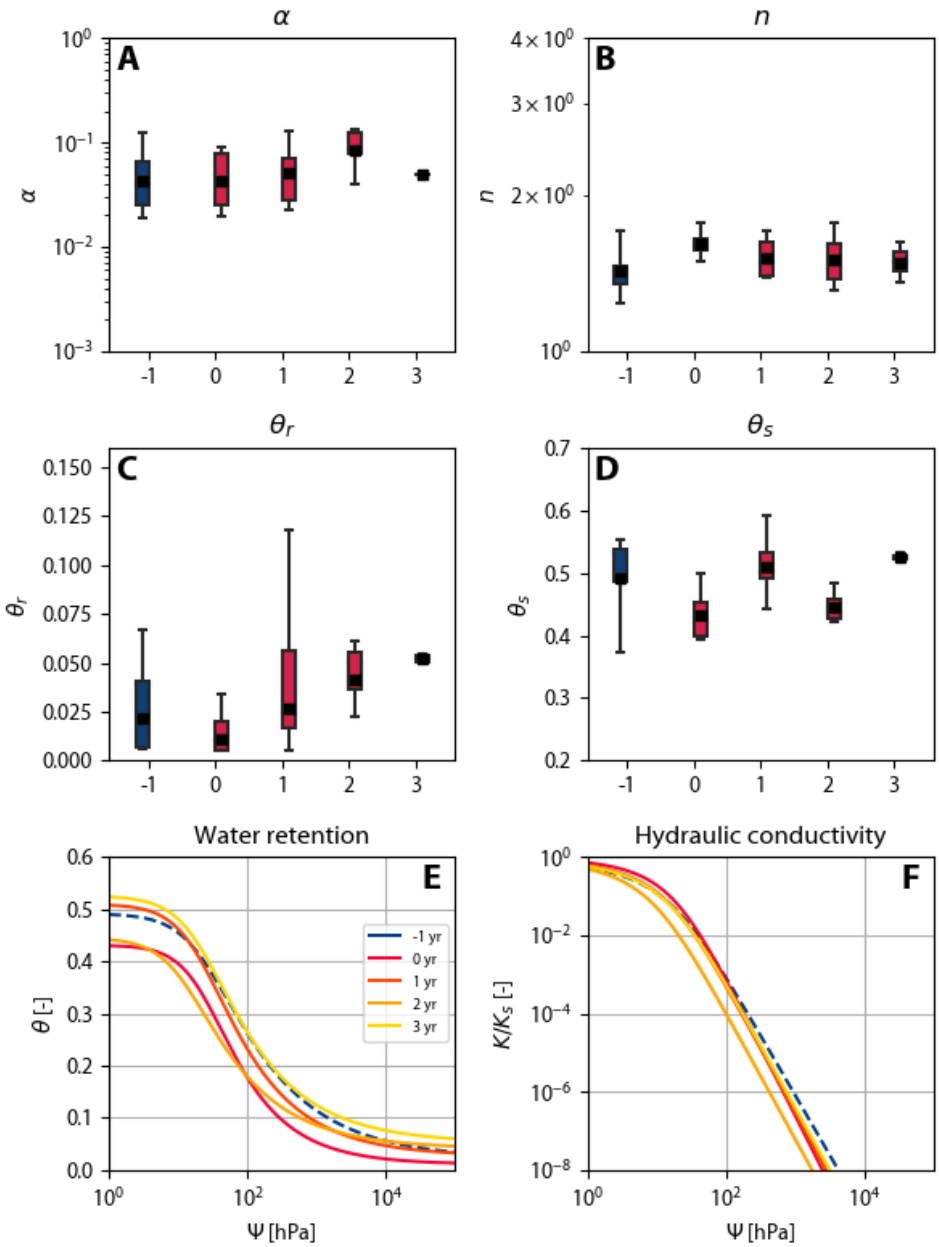

Figure 10. Compilation of best-fit Van Genuchten parameters showing distributions of inverse air entry pressure α (**A**), pore-size index n (**B**), residual soil-water content θ_r (**C**), and saturated soil-water content $\theta_{S,}$ (D) grouped by time since

burning. Blue box and whisker plots are for unburned samples, while red show burned samples. Boxes span the interquartile range, whiskers span the range of the data, black squares mark the geometric mean. Time category -1 is for unburned samples, 0 is for samples that were collected during the same year in which the fire occurred, 1 for samples collected in the year following the year the fire occurred, and so on. The corresponding mean soil-water retention curves for each time period are shown in (**E**) and mean normalized hydraulic conductivity curves in (**F**). Colors correspond to time since burning with dashed lines showing the mean unburned curves and solid lines showing mean burned curves.

When grouped by soil texture we see that SWRCs for burned soils shift to the left (such that soils release water over lower, and a narrower range of suction values), and the trend of increased n and α, and decreased storage terms θ_r and θ_S persists. Interestingly, the perturbation magnitude to the loam soils is greatest such that despite having distinct unburned SWRC curves, all post-fire curves collapse towards the sandy loam curve. The result is that following fire there is significantly less variability between soil textures. In the case of loam, the retention and conductivity behavior are perturbed to such a degree that the post-fire curve mimics that of a different soil texture (Figure 11).

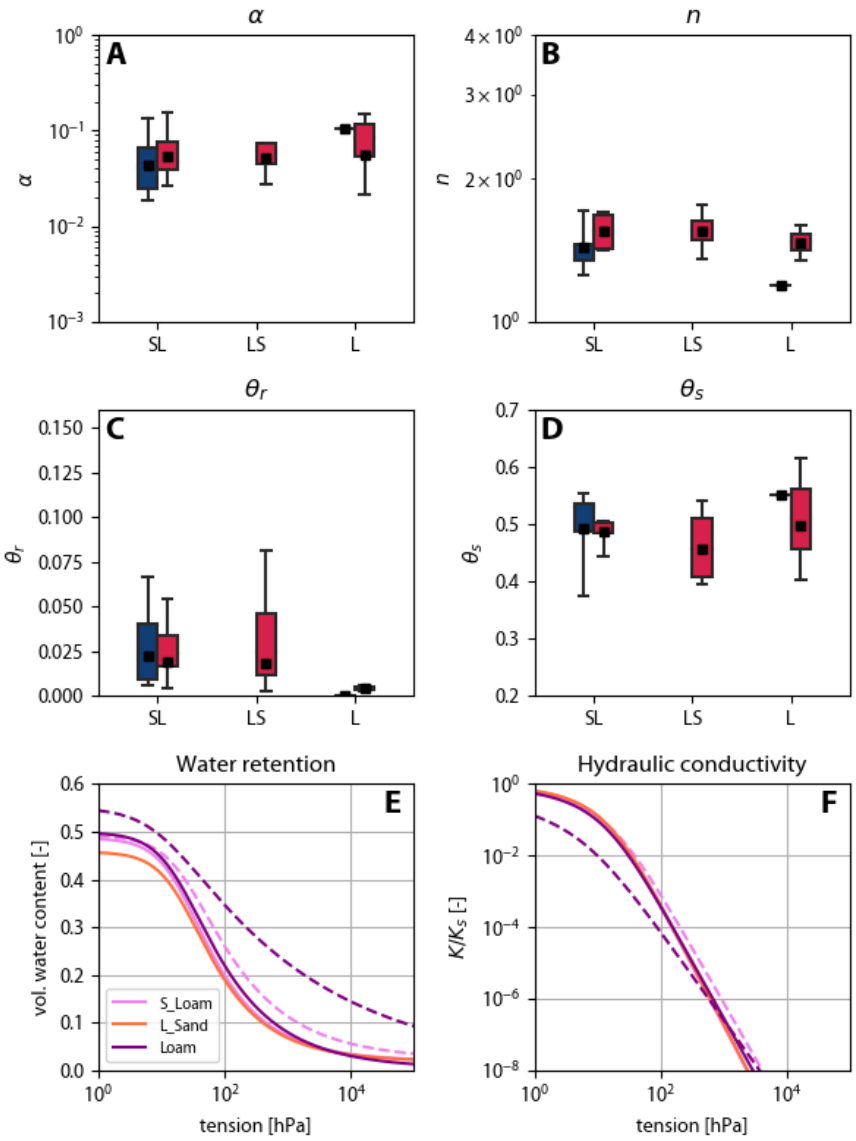

Figure 11. Compilation of best-fit Van Genuchten parameters showing distributions of inverse air entry pressure α (**A**), pore-size index n (**B**), residual soil-water content θ_r (**C**), and saturated soil-water content θ_S, (**D**) grouped by soil texture, where abbreviations are SL sandy loam, LS loamy sand, L loam. Blue box and whisker plots are for unburned samples, while red show burned samples. Boxes span the interquartile range, whiskers span the range of the data, black squares mark the geometric mean. The corresponding mean soil-water retention curves for each soil texture are shown in (**E**) and mean normalized hydraulic conductivity curves in (**F**). Colors correspond to soil texture with dashed lines showing the mean unburned curves and solid lines showing mean burned curves.

4.0: Impact of fire perturbations to SWRCs on runoff generation

To generalize the importance of the observed perturbations to SWRCs for rainfall runoff generation, we conducted numerical experiments with variably saturated flow modeling parameterized using the laboratory-based measurements of burned and unburned SWRCs. Specifically, laboratory SWRCs were applied to the computational framework from Thomas et al., 2021 that uses HYDRUS-1D (Šimůnek et al., 2009) to solve Richards (1931) equation and determine the sensitivity of runoff generation to changing SWRCs. In this framework we solve Richards equation in 1D for a small representative upper basin with a simulated rainfall rate. We diverge from the Thomas et al., 2021 framework in that we are not conducting the multi-annual climatological and recovery simulations to get initial conditions for the rainfall intensity-duration (ID) ensembles. Instead, we set an initial condition in which the fire-affected soil was 5 cm thick and set to the residual water content (θ_r) with *Ks* set to 1 mm/hr. The fire affected depth of 5 cm was chosen because soil temperatures are rarely >150°C for depths >5 cm during a fire (DeBano, 2000) or >100°C for depths >10 cm (Rengers et al., 2017) and the greatest depth to unaffected soil is typically ≤6 cm (Moody & Ebel, 2014; Nyman et al., 2013). The unaffected soil profile was set to a depth of 50 cm and is at field capacity (i.e., the point at which gravity dominated drainage slows/ceases) with *Ks* set to the Rosetta database value for loamy sand of ~43 mm/hr. The weathered bedrock below the unaffected soil was set to a porosity of half and a *Ks* two orders of magnitude lower than that of the unaffected soil, all other SWRC parameters were identical to the unaffected soil which were set to the Rosetta database values for loamy sand.

To build intuition of how our response variable of interest, rainfall runoff rate, changes as a function of Van Genunchten parameters, we performed a simple, one-at-a-time sensitivity analysis. While this analysis is not meant to be exhaustive or formal it does demonstrate to first order how potential changes in parameters controlling unsaturated soil behavior influence runoff and potential debris-flow generation. Initially we varied each Van Genuchten parameter individually across the range of our laboratory measured values while holding all others constant. We then changed all Van Genuchten parameters in concert to match the mean SWRC observed form the burned and unburned populations and to mimic the expected rainfall-runoff perturbation across our fire sites. Additionally, we performed simulations to match each fire specific perturbation and those results are presented in the supplementary figures (Figures S2-S8).

The main simulated output that we track is the runoff over a one-hour period of rainfall. We are most interested in runoff behavior during the first 15 minutes of rainfall as this timescale has been observed to be commonly related to debris flow initiation (Kean et al., 2011). Simulated rainfall rates were varied in 5 mm/hr increments from 0-100 mm/hr with 21 simulated storms per scenario.

4.1: Modeling Results

Our initial sensitivity analysis shows that perturbation to *n* has the least effect on runoff generation. Changes to α and θ_r have a moderate influence, while a decrease in θ_s exerts the strongest control on time to peak runoff at all rainfall rates relative to the base case of observed mean values (Figure 13).

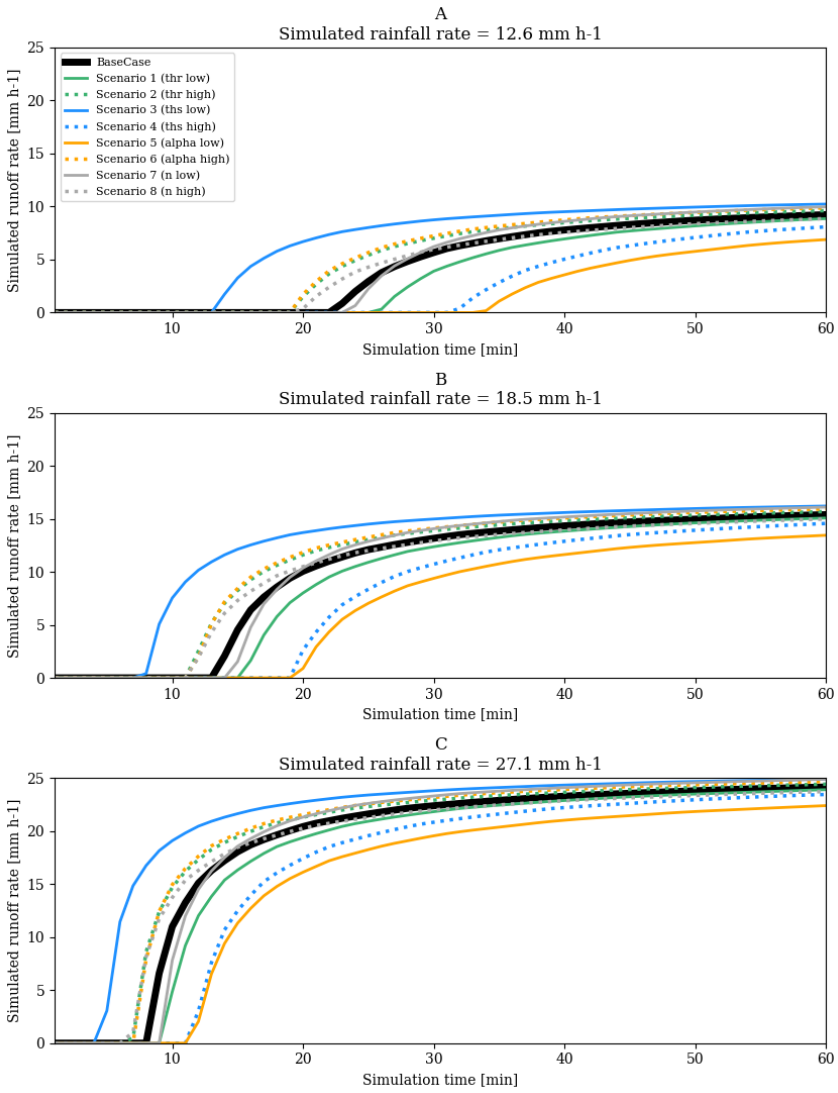

Figure 13. Sensitivity analysis of effects on runoff generation of varying each Van Genuchten parameter individually at different simulated rainfall rates. **A**: Simulated rainfall rate of 12.6 mm/hr. **B**: Simulated rainfall rate of 18.5 mm/hr. **C**: Simulated rainfall rate of 27.1 mm/hr

The runoff rate from simulations that use SWRC that match mean curves observed from the burned and unburned populations show a systematic increase in post-fire runoff relative to unburned soils, particularly over short time periods following initiation of rainfall. When the characteristic perturbations are applied to the simulation we see that the fully burned values (decreased θ_r and θ_s, increased α, and n) show the largest increase in runoff rate and delta runoff over time (Figure 14). Figure 15 shows the

volumetric water content (θ), $\Delta\theta$ / Δ time, and tension at different depths of the modeled 5 cm fire-affected soil over the duration of rainfall. The figure shows that the fire-affected soil does not reach saturated conditions at timescales relevant to debris-flow generation or during extended periods of rainfall that are beyond the scope of this project.

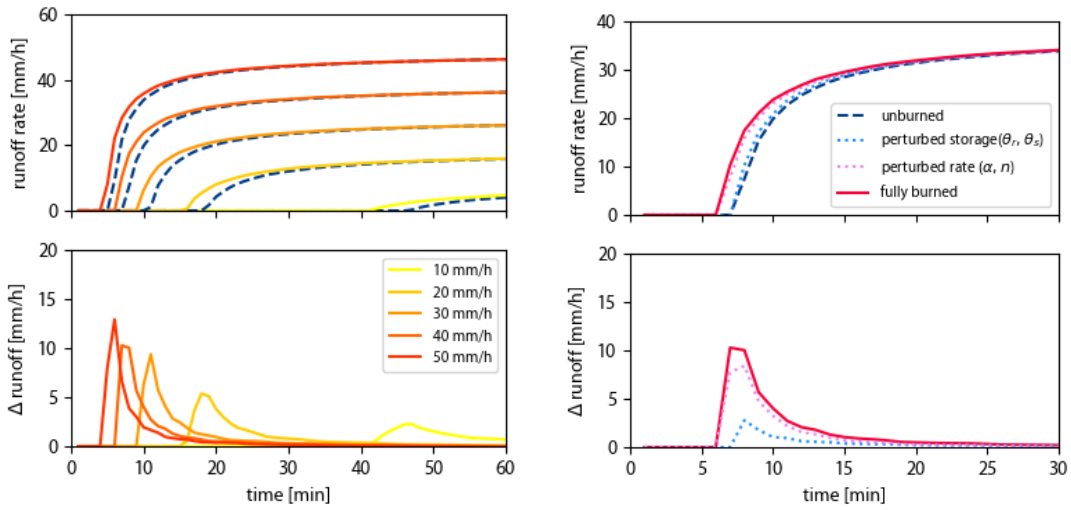

Figure 14. Delta runoff vs time by rainfall intensity (top two panels) and characteristic perturbation to VG parameters (bottom two panels).

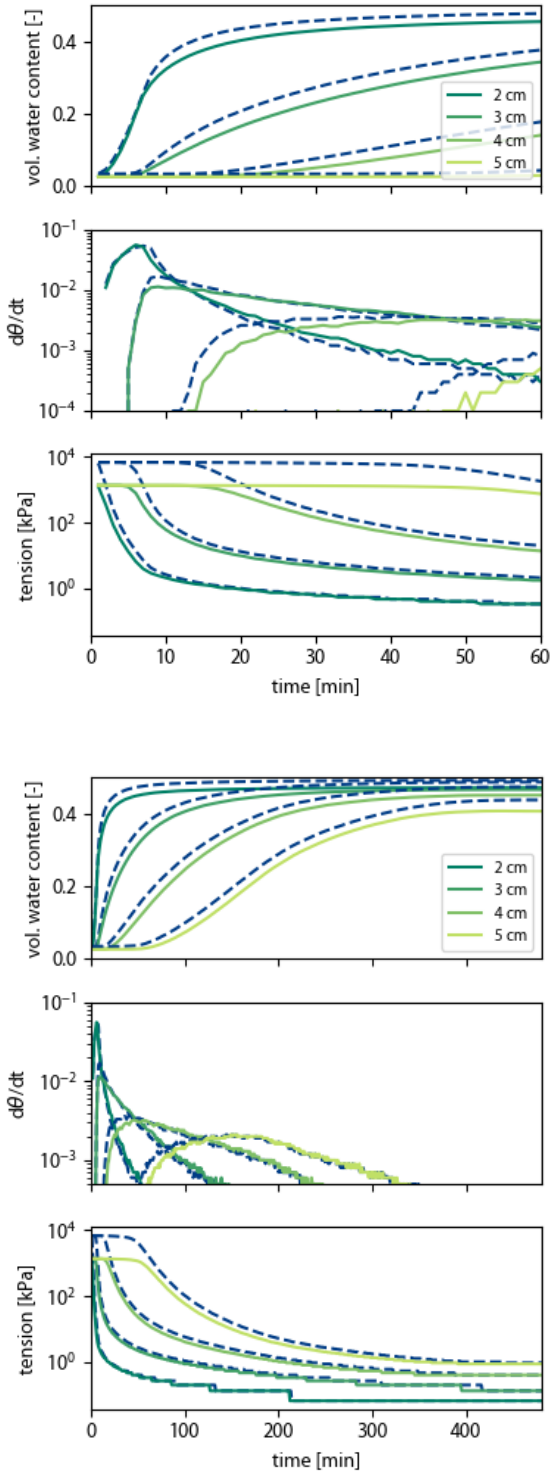

Figure 15. Top three panels: theta, tension and Δtheta vs time (0-60 minutes), Bottom three panels: theta, tension and Δtheta vs time (0-500 minutes). Simulated rainfall rate is 40 mm/hr.

5.0: Discussion

This study presents a large empirical data set of soil water retention curves (SWRC) from 43 unburned and 70 burned soil samples from seven studied fires. Measured SWRCs from both burned and unburned soils are well-fit using the Van Genuchten function (percent error of 2.3+/-1.0%, and 2.9+/-1.9%, respectively). While there is considerable variation in the post-fire perturbation to Van Genuchten parameters, there is a dominant trend across the data set. In most cases the rate of change terms, n and α both increased, while the storage terms, θ_r and θ_s, both decreased relative to mean unburned values. This characteristic perturbation causes the SWRC to steepen and shift to the left such that water retention is reduced across most suction values and soils drain at lower and narrower ranges of suction. In most cases there was a post-fire shift to the left in the SWRC when data is grouped by soil texture. The $K(\psi)$ curves seem to collapse to a narrower range of values than the unburned soils. This suggests a post-fire homogenization of soil structure, possibly due to the destruction of organic compounds and the incorporation of ash into the soil, as soil-water retention and hydraulic conductivity behavior become more representative of what is observed in well-sorted sands. When the entire data set is grouped by time, sublte post-fire trends of recovery can be identified across all Van Genuchten parameters except α, with parameters generally returning towards unburned values within the three-year time span investigated for most fire sites

Numerical simulations using HYDRUS 1-D show significantly enhanced runoff response to rainfall at the sub-hourly timescales relevant to debris-flow generation with the

characteristic perturbation of increased α, and n, and decreased θ_r and θ_s. Modeled results show an increase in runoff of >10 mm/hr within the first 10 minutes of simulated rainfall. This increased runoff due to post-fire perturbation to unsaturated soil-hydraulic parameters may be equally as significant as commonly observed post-fire reductions to *Ks.*

Post-fire perturbation to unsaturated soil-hydraulic properties appears to have an influence on runoff response to high-intensity short-duration rainfall and subsequent debris-flow generation. A greater understanding of the effects of post-fire change to Van Genuchten parameters is important due to the wide variety of applications. For example, Van Genuchten parameters are used in the Richards equation and in commonly used methods for analyzing field-measured minidisk infiltrometer data, such as Zhang's A1 and A2 (1997) equations for calculating *Ks* and sorptivity (Figure S1). These unsaturated soil-hydraulic properties are commonly assumed to be unaffected by wildfire and obtained from databases composed largely of unburned agricultural soils. While the post-fire variation in Van Genuchten parameters are variable, in many cases the observed perturbations impact infiltration to a similar degree as observed post-fire changes to *Ks* (Ebel and Moody, 2017). Our data and simulations show that the characteristic post-fire perturbation to Van Genuchten parameters does have a significant influence on time-to-ponding, runoff generation and debris-flow generation.

5.1: Conclusion

This study emphasizes the importance of quantifying post-wildfire perturbations to unsaturated soil-hydraulic properties and their influence on runoff response to rainfall. Our laboratory measurements of soil water retention curves were well fit by the Van Genuchten equation for both burned and unburned soils. Our results show considerable variation across the studied fires, however, there are characteristic trends in the post-fire perturbation to unsaturated soil properties across the dataset. In most cases, the Van Genuchten parameters that set the rate of change of soil moisture as a function of suction, *n* and α, increased relative to unburned values, while the water storage terms, θ_r and θ_s, both decreased (Table S3). Characteristically, SWRC, and $K(\psi)$ curves shift down and to the left post-burn, such that soils release water over lower, and a narrower range of suction values, and hydraulic conductivity generally decreases at higher tension values. When SWRCs are grouped by soil texture, this post-fire shift down and to the left of the SWRC, which was larger for loamy soils, had the effect of homogenizing SWRCs toward that seen for sandier soils. Similarly, the $K(\psi)$ curves seem to collapse to a narrower range of values than the unburned soils. Numerical simulations using HYDRUS 1-D show significantly enhanced post-fire runoff response to rainfall at the sub-hourly timescales relevant to debris flow generation with the characteristic perturbation of increased α, and n, and decreased θ_r and θ_s. Modeled results show an increase in runoff of >10 mm/hr within the first 10 minutes of simulated rainfall. This increased runoff due to post-fire perturbation to unsaturated soil-hydraulic parameters may be equally as significant as commonly observed post-fire reductions to *Ks.* These simulations suggest

that the most commonly observed perturbations to SWRCs decrease time to ponding and strongly increase runoff generation at the sub-hourly timescales relevant to flash flooding and debris-flow initiation by rainfall runoff. These results highlight that field constraints on soil-hydraulic properties beyond just the saturated hydraulic conductivity are critical to more accurate prediction of rapid rainfall runoff following fire. Van Genuchten parameters taken from agricultural databases of unburned soils based on mapped soil textures are generally congruent with measured unburned values. However, measured parameters from burned soils consistently diverge from unburned database values (Figure S9). Directly measuring the characteristic post-fire perturbation to Van Genuchten parameters may improve accuracy when quantifying potential runoff response to rainfall and interpreting field measurements of infiltration rates and subsequent calculations of *Ks* and sorptivity. The large database of such measurements presented here provides an important step towards increasing our understanding of the magnitude of expected post-fire perturbations to unsaturated soil-hydraulic properties and their influence on flash-flood and debris-flow hazards.

References Cited

Alauzis, M. V., M. J. Mazzarino, E. Raffaele, and L. Roselli (2004), Wild- fires in NW Patagonia: Long-term effects on a Nothofagus forest soil, For. Ecol. Manage., 192, 131–142.

Are, K. S., G. A. Oluwatosin, O. D. Adeyolanu, and A. O. Oke (2009), Slash and burn effect on soil quality of an Alfisol: Soil physical proper- ties, Soil Tillage Res., 103, 4–10.

ASTM International. (2016). *Test Methods for Determination of the Soil Water Characteristic Curve for Desorption Using Hanging Column, Pressure Extractor, Chilled Mirror Hygrometer, or Centrifuge*. ASTM International. https://doi.org/10.1520/D6836-16

Badia, D., and C. Marti (2003), Plant ash and heat intensity effects on chemical and physical properties of two contrasting soils, Arid Land Res. Manage., 17, 23–41.

Boix-Fayos, C. (1997), The roles of texture and structure in the water reten- tion capacity of burnt Mediterranean soils with varying rainfall, Catena, 31, 219–236.

Breitmeyer, R. J., & Fissel, L. (2017). Uncertainty of soil water characteristic curve measurements using an automated evaporation technique. *Vadose Zone Journal*, *16*(13), 1-11.

Cannon, S. H., Boldt, E. M., Laber, J. L., Kean, J. W., & Staley, D. M. (2011). Rainfall intensity–duration thresholds for postfire debris-flow emergency-response planning. *Natural Hazards*, *59*(1), 209–236. https://doi.org/10.1007/s11069-011-9747-2

Cannon, S. H., Gartner, J. E., Rupert, M. G., Michael, J. A., Rea, A. H., & Parrett, C. (2010). Predicting the probability and volume of postwildfire debris flows in the intermountain western United States. *Geological Society of America Bulletin*, *122*(1–2), 127–144. https://doi.org/10.1130/B26459.1

Cannon, S. H., Gartner, J. E., Rupert, M. G., Michael, J. A., Staley, D. M., & Worstell, B. B. (2009). *Emergency assessment of postfire debris-flow hazards for the 2009 Station Fire, San Gabriel Mountains, Southern California*. US Geological Survey. https://pubs.er.usgs.gov/publication/ofr20091227

Cannon, S. H., & DeGraff, J. (2009). The increasing wildfire and post-fire debris-flow threat in western USA, and implications for consequences of climate change. In *Landslides–disaster risk reduction* (pp. 177-190). Springer, Berlin, Heidelberg.

Cannon, S. H., Gartner, J. E., Wilson, R. C., Bowers, J. C., & Laber, J. L. (2008). Storm rainfall conditions for floods and debris flows from recently burned areas in southwestern Colorado and southern California. *Geomorphology*, *96*(3–4), 250–269. https://doi.org/10.1016/j.geomorph.2007.03.019

Carsel, R. F., & Parrish, R. S. (1988). Developing joint probability distributions of soil water retention characteristics. *Water resources research*, *24*(5), 755-769.

Certini, G. (2005). Effects of fire on properties of forest soils: a review. *Oecologia*, *143*(1), 1-10.

DeBano, L. F. (2000). The role of fire and soil heating on water repellency in wildland environments: a review. *Journal of hydrology*, *231*, 195-206.

DiBiase, R. A., & Lamb, M. P. (2020). Dry sediment loading of headwater channels fuels post-wildfire debris flows in bedrock landscapes. *Geology*, *48*(2), 189–193. https://doi.org/10.1130/G46847.1

Ebel, B. A. (2020a). Temporal evolution of measured and simulated infiltration following wildfire in the Colorado Front Range, USA: Shifting thresholds of runoff generation and hydrologic hazards. *Journal of Hydrology*, *585*, 124765. https://doi.org/10.1016/j.jhydrol.2020.124765

Ebel, B. A. (2020b). Temporal evolution of measured and simulated infiltration following wildfire in the Colorado Front Range, USA: Shifting thresholds of runoff generation and hydrologic hazards. *Journal of Hydrology*, *585*, 124765. https://doi.org/10.1016/j.jhydrol.2020.124765

Ebel, B. A., & Moody, J. A. (2017). Synthesis of soil-hydraulic properties and infiltration timescales in wildfire-affected soils: Synthesis of soil-hydraulic properties in wildfire-affected soils. *Hydrological Processes*, *31*(2), 324–340. https://doi.org/10.1002/hyp.10998

Ebel, B. A., & Moody, J. A. (2020a). Parameter estimation for multiple post-wildfire hydrologic models. *Hydrological Processes*, *34*(21), 4049–4066. https://doi.org/10.1002/hyp.13865

Ebel, B. A., & Moody, J. A. (2020b). Parameter estimation for multiple post-wildfire hydrologic models. *Hydrological Processes*, *34*(21), 4049–4066. https://doi.org/10.1002/hyp.13865

Ebel, B. A., Moody, J. A., & Martin, D. A. (2012). Hydrologic conditions controlling runoff generation immediately after wildfire: HYDROLOGIC CONDITIONS CONTROLLING RUNOFF AFTER WILDFIRE. *Water Resources Research*, *48*(3). https://doi.org/10.1029/2011WR011470

Ebel, B. A., Moody, J. A., & Martin, D. A. (2022). Post-fire temporal trends in soil-physical and hydraulic properties and simulated runoff generation: Insights from different burn severities in the 2013 Black Forest Fire, CO, USA. *Science of The Total Environment*, *802*, 149847. https://doi.org/10.1016/j.scitotenv.2021.149847

Farrick, K. K., Wuddivira, M. N., & Martin, O. (2019). Estimation of soil texture from permanent wilting point measured with a chilled-mirror dewpoint technique. *Journal of Plant Nutrition and Soil Science*, *182*(1), 119-125.

Felling, G., Myers, A., & McCoy, S. W. (2019). *Post-fire debris-flow hazard analysis for Interstate 80, Truckee River Canyon, near the California-Nevada state line, USA.* 8

Fissel, L., & Breitmeyer, R. J. (2017). Evaluation of Uncertainty for Soil Water Characteristic Curve Measurements and the Implications for Predicting the Hydro-Mechanical Behavior of Unsaturated Soils. *Geotechnical Frontiers 2017*, 579–588. https://doi.org/10.1061/9780784480472.061

Fredlund, D. G. (2019). State of practice for use of the soil-water characteristic curve (SWCC) in geotechnical engineering. *Canadian Geotechnical Journal*, *56*(8), 1059-1069.
Iglesias, V., Balch, J. K., & Travis, W. R. (2022). U.S. fires became larger, more frequent, and more widespread in the 2000s. *Science Advances*, *8*(11), eabc0020. https://doi.org/10.1126/sciadv.abc0020

Giovannini, G., and S. Lucchesi (1997), Modifications induced in soil phys- ico-chemical parameters by experimental fires at different intensities, Soil Sci., 162, 479–486.

Gonzalez-Pelayo, O., V. Andreu, J. Campo, E. Gimeno-Garcia, and J. L. Rubio (2006), Hydrological properties of a Mediterranean soil burned with different intensities, Catena, 68, 186–196.

Iverson, R. M. (1997). The physics of debris flows. *Reviews of Geophysics*, *35*(3), 245–296.

Kean, J. W., McCoy, S. W., Tucker, G. E., Staley, D. M., & Coe, J. A. (2013). Runoff-generated debris flows: Observations and modeling of surge initiation, magnitude, and frequency. *Journal of Geophysical Research: Earth Surface*, *118*(4), 2190–2207. https://doi.org/10.1002/jgrf.20148

Kean, J. W., McGuire, L. A., Rengers, F. K., Smith, J. B., & Staley, D. M. (2016). Amplification of postwildfire peak flow by debris. *Geophysical Research Letters*, 2016GL069661. https://doi.org/10.1002/2016GL069661

Kean, J. W., & Staley, D. M. (2011). Direct measurements of the hydrologic conditions leading up to and during post-fire debris flow in southern California, USA. *Debris-Flow Hazards Mitigation, Mechanics, Prediction, and Assessment, Edited by R. Genevois, DL Hamilton, and A. Prestininzi*, 685–694.

Kitzberger, T., E. Raffaele, K. Heinemann, M. J. Mazzarino, and P. Harcombe (2005), Effects of fire severity in a north Patagonian subalpine forest, J. Veget. Sci., 16, 5–12.

Mallik, A. U., C. H. Gimingham, and A. A. Rahman (1984), Ecological effects of heather burning, I. Water infiltration, moisture retention and porosity of surface soils, J. Ecol., 72, 767–776.

Martínez, S. I., Contreras, C. P., Acevedo, S. E., & Bonilla, C. A. (2022). Unveiling soil temperature reached during a wildfire event using ex-post chemical and hydraulic soil analysis. *Science of The Total Environment*, *822*, 153654.

Mataix-Solera, J., Cerdà, A., Arcenegui, V., Jordán, A., & Zavala, L. M. (2011). Fire effects on soil aggregation: a review. *Earth-Science Reviews*, *109*(1-2), 44-60.

McCoy, S. W., Kean, J. W., Coe, J. A., Staley, D. M., Wasklewicz, T. A., & Tucker, G. E. (2010). Evolution of a natural debris flow: In situ measurements of flow dynamics, video imagery, and terrestrial laser scanning. *Geology*, *38*(8), 735–738.

METER Group. (2015). Operation Manual HYPROP.

METER Group. (2018). WP4C Dew Point Potentio Meter Operator's Manual.

McGuire, L. A., Kean, J. W., Staley, D. M., Rengers, F. K., & Wasklewicz, T. A. (2016). Constraining the relative importance of raindrop- and flow-driven sediment transport *Geophysical Research: Earth Surface*, *121*(11), 2211–2237. https://doi.org/10.1002/2016JF003867

Mirus, B. B. (2015). Evaluating the importance of characterizing soil structure and horizons in parameterizing a hydrologic process model. *Hydrological Processes*, *29*(21), 4611-4623.

Mirus, B. B., & Loague, K. (2013). How runoff begins (and ends): Characterizing hydrologic response at the catchment scale. *Water Resources Research*, *49*(5), 2987-3006.

Moody, J. A., Ebel, B. A., Nyman, P., Martin, D. A., Stoof, C., & McKinley, R. (2016a). Relations between soil hydraulic properties and burn severity. *International Journal of Wildland Fire*, *25*(3), 279. https://doi.org/10.1071/WF14062

Moody, J. A., Ebel, B. A., Nyman, P., Martin, D. A., Stoof, C., & McKinley, R. (2016b). Relations between soil hydraulic properties and burn severity. *International Journal of Wildland Fire*, *25*(3), 279. https://doi.org/10.1071/WF14062

Moody, J. A., & Ebel, B. A. (2014). Infiltration and runoff generation processes in fire-affected soils. *Hydrological Processes*, *28*(9), 3432-3453.

Moody, J. A., Kinner, D. A., & Úbeda, X. (2009). Linking hydraulic properties of fire-affected soils to infiltration and water repellency. *Journal of Hydrology*, *379*(3), 291–303. https://doi.org/10.1016/j.jhydrol.2009.10.015

Mualem, Y. (1976). A new model for predicting the hydraulic conductivity of unsaturated porous media. *Water Resources Research*, *12*(3), 513–522. https://doi.org/10.1029/WR012i003p00513

Nyman, P., Sheridan, G. J., Moody, J. A., Smith, H. G., Noske, P. J., & Lane, P. N. J. (2013). Sediment availability on burned hillslopes. *Journal of Geophysical Research: Earth Surface*, *118*(4), 2451–2467. https://doi.org/10.1002/jgrf.20152

Pereira, P., Francos, M., Brevik, E. C., Ubeda, X., & Bogunovic, I. (2018). Post-fire soil management. *Current Opinion in Environmental Science & Health*, *5*, 26-32.

Peters, A., & Durner, W. (2008). Simplified evaporation method for determining soil hydraulic properties. *Journal of Hydrology*, *356*(1-2), 147-162.

Radeloff, V. C., Helmers, D. P., Kramer, H. A., Mockrin, M. H., Alexandre, P. M., Bar-Massada, A., ... & Stewart, S. I. (2018). Rapid growth of the US wildland-urban interface raises wildfire risk. *Proceedings of the National Academy of Sciences*, *115*(13), 3314-3319.

Rengers, F. K., McGuire, L. A., Kean, J. W., Staley, D. M., & Hobley, D. E. J. (2016). Model simulations of flood and debris flow timing in steep catchments after wildfire. *Water Resources Research*, *52*(8), 6041–6061. https://doi.org/10.1002/2015WR018176

Rengers, F. K., McGuire, L. A., Kean, J. W., Staley, D. M., & Youberg, A. M. (2019a). Progress in simplifying hydrologic model parameterization for broad applications to post-wildfire flooding and debris-flow hazards. *Earth Surface Processes and Landforms*, *44*(15), 3078–3092.https://doi.org/10.1002/esp.4697

Rengers, F. K., McGuire, L. A., Kean, J. W., Staley, D. M., & Youberg, A. M. (2019b). Progress in simplifying hydrologic model parameterization for broad applications to post-wildfire f looding and debris-flow hazards. *Earth Surface Processes and Landforms*, *44*(15), 3078–3092. https://doi.org/10.1002/esp.4697

Richards, L. A. (1931). Capillary conduction of liquids through porous mediums. *Physics*, *1*(5), 318-333.

Schaap, M. G., Leij, F. J., & Van Genuchten, M. T. (2001). Rosetta: A computer program for estimating soil hydraulic parameters with hierarchical pedotransfer functions. *Journal of hydrology*, *251*(3-4), 163-176.

Shokrana, M. S. B., & Ghane, E. (2020). Measurement of soil water characteristic curve using HYPROP2. *MethodsX*, *7*, 100840.

Silva, J. S., F. C. Rego, and S. Mazzoleni (2006), Soil water dynamics after fire in a Portuguese Shrubland, Int. J. Wildland Fire, 15, 99–111.

Šimůnek, J., & Hopmans, J. W. (2009). Modeling compensated root water and nutrient uptake. *Ecological modelling*, *220*(4), 505-521.

Staley, D. M., Negri, J. A., Kean, J. W., Laber, J. L., Tillery, A. C., & Youberg, A. M. (2017). Prediction of spatially explicit rainfall intensity–duration thresholds for post-fire debris-flow generation in the western United States. *Geomorphology*, *278*, 149-162.

Staley, D. M., Kean, J. W., Cannon, S. H., Schmidt, K. M., & Laber, J. L. (2013). Objective definition of rainfall intensity–duration thresholds for the initiation of post-fire debris flows in southern California. *Landslides*, *10*(5), 547-562.

Staley, D. M., Wasklewicz, T. A., & Kean, J. W. (2014). Characterizing the primary material sources and dominant erosional processes for post-fire debris-flow initiation in a headwater basin using multi-temporal terrestrial laser scanning data. *Geomorphology*, *214*, 324-338.

Stoof, C. R., J. G. Wesseling, and C. J. Ritsema (2010), Effects of fire and ash on soil water retention, Geoderma, 159, 276–285.

Thomas, M. A., Rengers, F. K., Kean, J. W., McGuire, L. A., Staley, D. M., Barnhart, K. R., & Ebel, B. A. (2021). Postwildfire soil-hydraulic recovery and the persistence of debris flow hazards. *Journal of Geophysical Research: Earth Surface*, *126*(6), e2021JF006091.

Ulery, A. L., and R. C. Graham (1993), Forest fire effects on soil color and texture, Soil Sci. Soc. Am. J., 57, 135–140.

Westerling, A. L., Hidalgo, H. G., Cayan, D. R., & Swetnam, T. W. (2006). Warming and Earlier Spring Increase Western U.S. Forest Wildfire Activity. *Science*, *313*(5789), 940–943. https://doi.org/10.1126/science.1128834

Williams, A. P., Abatzoglou, J. T., Gershunov, A., Guzman-Morales, J., Bishop, D. A., Balch, J. K., & Lettenmaier, D. P. (2019). Observed impacts of anthropogenic climate change on wildfire in California. *Earth's Future*, *7*(8), 892-910.

Van Genuchten, M. T. (1980). A closed-form equation for predicting the hydraulic conductivity of unsaturated soils. *Soil science society of America journal*, *44*(5), 892-898

Zhang, R. (1997). Infiltration models for the disk infiltrometer. *Soil Science Society of America Journal*, *61*(6), 1597-1603.

Supplemental Materials

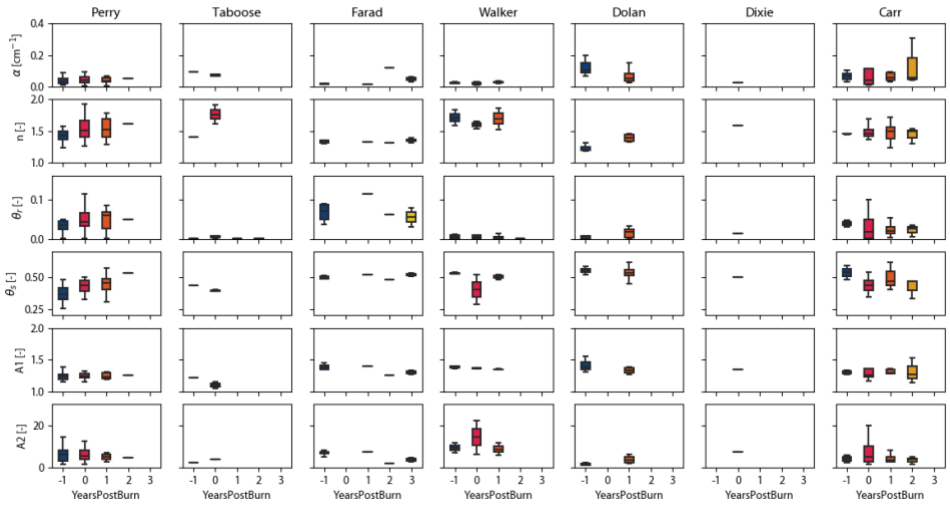

Figure S1. Visual representation of the entire dataset that follows in tables S1 and S3. This figure shows the perturbation to Van Genuchten parameters for all unburned and burned soil samples over several years since the fires (where applicable), as well as A1 and A2 (Zhang, 1997) calculated with measured Van Genuchten parameters. 1/A2 is proportional to *Ks*, and 1/A1 is proportional to sorptivity. Blue box and whisker plots are for unburned samples, while red show all burned samples. Boxes span the interquartile range, whiskers span the range of the data, black squares mark the geometric mean.

Fire	Sample Name	Years	Burned	Lon	Lat	Location	Bad	SWCC alpha	SWCC n	SWCC th_r	SWCC th_s
Perry	Sample1A_PerryCanyon	18	0	-119.5811043	39.84473753	1A	0	0.0251	1.414	0.033962685	0.373962685
Perry	Perryfire1A_07262020_new	19	0	-119.5811043	39.84473753	1A	0	0.0148	1.352	0.042128514	0.353975904
Perry	PerryFire1A_07032019	19	0	-119.5811043	39.84473753	1A	0	0.0211	1.573	-0.054779116	0.268875502
Perry	PerryFire1A_02222019_adj	18	0	-119.5811043	39.84473753	1A	0	0.0742	1.169	0.014225379	0.323622969
Perry	PerryFire2A_11142018_adj	18	0	-119.5927558	39.8487745	2A	0	0.0363	1.287	0.035834512	0.346878689
Perry	200820_PerryFire2A_091118A	18	0	-119.5927558	39.8487745	2A	0	0.0192	1.45	0.037630522	0.327831325
Perry	PerryFire2A_07172019	19	0	-119.5927558	39.8487745	2A	0	0.0152	1.569	-0.050160643	0.251967871
Perry	PerryFire2A_02212019_adj	18	0	-119.5927558	39.8487745	2A	0	0.0879	1.257	0.088594249	0.433935614
Perry	PerryFire2A_07262020_new	19	0	-119.5927558	39.8487745	2A	0	0.0194	1.384	0.043895582	0.34686747
Perry	200820_PerryFire3A_092118	18	0	-119.5962015	39.84995853	3A	0	0.0115	1.517	0.050235904	0.383328273
Perry	PerryFire3A_11212018_adj	18	0	-119.5962015	39.84995853	3A	0	0.026	1.519	0.033518747	0.408860113
Perry	PerryFire3A_09172020_new	19	0	-119.5962015	39.84995853	3A	0	0.0167	1.488	0.027349398	0.373654618
Perry	PerryFire3A_03122019_adj	18	0	-119.5962015	39.84995853	3A	0	0.0415	1.486	0.077420519	0.555452648
Perry	200820_PerryFire4A_1032018	18	0	-119.5990268	39.85049883	4A	0	0.0224	1.379	0.036726465	0.324919236
Perry	PerryFire4A_01092019	18	0	-119.5990268	39.85049883	4A	0	0.0442	1.237	0.030674493	0.321437545
Perry	PerryFire4A_03262019_adj	18	0	-119.5990268	39.85049883	4A	0	0.0516	2.1	0.026023808	0.37927682
Perry	190602_PerryFire5A_01162019_restart	18	0	-119.6092745	39.86136647	5A	0	0.0107	1.311	0.533	0.011
Perry	PerryFire5A_03292019_adj	18	0	-119.6092745	39.86136647	5A	0	0.079	1.465	0.021857447	0.438805238
Perry	PerryFire5A_2020	20	0	-119.6092745	39.86136647	5A	0	0.0586	1.389	0.015662651	0.33124498
Perry	PerryFire6A_101618	18	0	-119.6026798	39.85314642	6A	0	0.033	1.463	0.087505474	0.460075755
Perry	PerryFire6A_09052020_new	19	0	-119.6026798	39.85314642	6A	0	0.1125	1.412	0.104779116	0.48184739
Perry	Sample 1B_PerryCanyon	18	1	-119.5813715	39.84469553	1B	0	0.0332	1.524	0.047937547	0.42251586
Perry	PerryFire1B_11142018_adj	18	1	-119.5813715	39.84469553	1B	0	0.0457	1.58	0.040907728	0.428859535
Perry	PerryFire1B_02152019.adj	18	1	-119.5813715	39.84469553	1B	0	0.1736	1.262	0.096156269	0.500493619
Perry	PerryFire1B_07092019	19	1	-119.5813715	39.84469553	1B	0	0.00321	3.584	-0.077710843	0.270843373
Perry	perry_fire_1B_07162020_new	19	1	-119.5813715	39.84469553	1B	0	0.0262	1.438	0.085301205	0.479598394
Perry	PerryFire2B_111222018_adj	18	1	-119.5924838	39.84869052	2B	0	0.1238	1.351	0.021984687	0.48780798
Perry	PerryFire2B091118	18	1	-119.5924838	39.84869052	2B	0	0.0107	1.412	0.103253012	0.500120482
Perry	perry_fire_2B_07162020_new	19	1	-119.5924838	39.84869052	2B	0	0.0669	1.341	0.084578313	0.496305221
Perry	PerryFire2B_03072019	18	1	-119.5924838	39.84869052	2B	0	0.163	1.435	0.044437134	0.471987335
Perry	PerryFire3B_12042018_adj	18	1	-119.5960562	39.84982668	3B	0	0.0284	1.413	0.031645192	0.368713465
Perry	200820_Perryfire3B_09212018	18	1	-119.5960562	39.84982668	3B	0	0.00286	2.703	0.056659386	0.441840109
Perry	Perryire3B_8052020_new	19	1	-119.5960562	39.84982668	3B	0	0.0305	1.466	0.063534137	0.474859438
Perry	PerryFire3B_03142019	18	1	-119.5960562	39.84982668	3B	0	0.0294	1.762	0.028434528	0.392450592
Perry	PerryFire4B_01092019_adj	19	1	-119.5991693	39.85055868	4B	0	0.0517	1.592	0.028286551	0.436559644
Perry	200820_PerryFire4B_1032018	18	1	-119.5991693	39.85055868	4B	0	0.0402	1.63	0.055771971	0.466253898
Perry	Perryfire4B_8052020_new	19	1	-119.5991693	39.85055868	4B	0	0.0345	1.288	0.020803213	0.30686747
Perry	PerryFire4B_03282019_adj	18	1	-119.5991693	39.85055868	4B	0	0.0916	1.397	0.149890337	0.630894353
Perry	Perryfire4B_8082020_new	18	1	-119.5991693	39.85055868	4B	0	0.0385	1.392	0.113614458	0.421004016
Perry	Perry Canyon Sample 5B082918	18	1	-119.6091552	39.86117142	5B	0	0.0163	2.206	0.042938141	0.321452197
Perry	PerryFire5B_02052019_adj	18	1	-119.6091552	39.86117142	5B	0	0.022	1.525	0.032622181	0.391738647
Perry	PerryFire5B_091720_redo	19	1	-119.6091552	39.86117142	5B	0	0.0657	1.662	0.056385542	0.574538153
Perry	PerryFire5B_2020	20	1	-119.6091552	39.86117142	5B	0	0.0503	1.619	0.049477912	0.53188755
Perry	200820_PerryFire6B_1042018	18	1	-119.6027019	39.85310988	6B	0	0.0426	1.931	-0.012128514	0.377148594
Perry	PerryFire6B_02122019_adj	18	1	-119.6027019	39.85310988	6B	0	0.0494	1.509	0.034676715	0.458251012
Perry	PerryFire6B_09052020_new	19	1	-119.6027019	39.85310988	6B	0	0.0362	1.782	0.063092369	0.431084337
Farad	FaradFireFF1_2020	20	0	-120.02302	39.45629	F50	0	0.0157	1.318	0.085662651	0.422931727
Farad	Farad2_10252018	18	0	-120.0231	39.45638	F51	0	0.0171	1.322	0.038	0.51
Farad	FaradFF2_2019	19	0	-120.0231	39.45638	F51	0	0.0232	1.306	0.089477912	0.505140562
Farad	FF2_2020	20	0	-120.0231	39.45638	F51	0	0.019	1.448	0.054016064	0.50875502
Farad	FaradFireFF3_2019	19	1	-120.01918	39.45372	F54	0	0.1178	1.311	0.06124498	0.482771084
Farad	FF3_2020	20	1	-120.01918	39.45372	F54	0	0.0634	1.32	0.079558233	0.529317269
Farad	Farad4_10252018	18	1	-120.01894	39.45299	F57	0	0.0163	1.325	0.113975904	0.522128514
Farad	F4	18	1	-120.01894	39.45299	F57	0	0.0294	1.444	0.12188755	0.659036145
Farad	F4_2020	20	1	-120.01894	39.45299	F57	0	0.0337	1.392	0.029879518	0.508835341
Carr	CFBC1_01192019	18	1	-122.6359141	40.60900772	DL_I12	0	0.2697	1.476	0.033935743	0.342690763
Carr	CFBC_1_2019	19	1	-122.6359141	40.60900772	DL_I12	0	0.0368	1.566	0.024216867	0.484257028
Carr	CFBC_1_2020	20	1	-122.6359141	40.60900772	DL_I12	0	0.0392	1.493	0.035582329	0.46815261
Carr	CFBC2_01292019	18	1	-122.63614	40.60902	CFBC_I10	0	0.02	1.365	0.099799197	0.415060241
Carr	CFBC_2_2019	19	1	-122.63614	40.60902	CFBC_I10	0	0.029	1.716	0.004457831	0.429919679
Carr	CFBC_2_2020	20	1	-122.63614	40.60902	CFBC_I10	0	0.0551	1.533	0.006385542	0.328273092

Table S1. Fire and sample name, location, burned or unburned status, HYROP measured Van Genuchten values

Fire	Sample Name	Years	Burned	Lon	Lat	Location	Bad	SWCC alpha	SWCC n	SWCC th_r	SWCC th_s
Walker	WU1	20	0	-120.625138	40.154221	campsite	0	0.0211	1.832	0.013	0.538
Walker	W_U2_20	20	0	-120.625138	40.154221	campsite	0	0.0288	1.589	0.01	0.525
Walker	W1	19	1	-120.66516	40.08923	W26/rain	0	0.00861	1.659	0.009	0.286
Walker	W1	20	1	-120.66516	40.08923	W26/rain	0	0.0343	1.53	0.004	0.522
Walker	W2	19	1	-120.66972	40.04607	W25	0	0.0307	1.541	0.009	0.517
Walker	W2	20	1	-120.66972	40.04607	W25	0	0.0217	1.867	0.014	0.483
Taboose	T1	19	1	-118.36172	37.03405	T50	0	0.0662	1.612	0.008	0.401
Taboose	T3	19	1	-118.36215	37.03482	T3	0	0.079	1.915	0.007	0.389
Taboose	T4	20	0	-118.36215	37.03482	T4	0	0.0576	1.462	0.01	0.43
Taboose	T6	19	0	-118.35761	37.02358	T61	0	0.092	1.414	0.008	0.435
Dixie	DX2_SFC_21	21	1	-121.31415	39.95029	Granite	0	0.0273	1.589	0.015	0.5
Dixie	DX1_sfc_21	21	1	-121.28274	40.00727	Chips	0	0.0474	1.3	0.005	0.656
Dixie	DX2_10cm_21	21	0	-121.31415	39.95029	Granite	0	0.035	1.599	0.015	0.512
Dixie	DX2_25cm_21	21	0	-121.31415	39.95029	Granite	0	0.023	1.621	0.018	0.5
Dixie	DX1_15cm_21	21	0	-121.28274	40.00727	Chips	0	0.0217	1.41	0.017	0.588
Dixie	DX1_35cm_21	21	0	-121.28274	40.00727	Chips	0	0.0223	1.442	0.019	0.588
Dolan	D2U	21	0	-121.3582762	35.98993316	Nacimiento	0	0.0683	1.313	0.024	0.522
Dolan	D3U	21	0	-121.592333	36.088206	Cathedral (U)	0	0.1042	1.193	0.0001	0.55
Dolan	D4U	21	0	-121.434398	35.992731	Mill	0	0.1978	1.195	0.002	0.585
Dolan	D1_SWM	21	1	-121.36477	36.0001	Hot Creek	0	0.064	1.325	0.026	0.53
Dolan	D1	21	1	-121.361167	35.999475	Nacimiento	0	0.1486	1.348	0.016	0.615
Dolan	D3	21	1	-121.434409	35.992514	Mill	0	0.0269	1.457	0.021	0.536
Dolan	D4	21	1	121.434398	35.992731	Mill	0	0.0381	1.449	0.033	0.451
Dolan	D6E	21	1	-121.592484	36.093593	Cathedral	0	0.0546	1.487	0.03	0.575
Dolan	D6W	21	1	-121.591955	36.093171	Cathedral	0	0.1157	1.244	0.01	0.595

Table S1 (cont). Fire and sample name, location, burned or unburned status, HYROP measured Van Genuchten

Fire	USDA WSS Map unit name	Map unit symbol	WSS soil texture	Rosetta texture	Rosetta alpha	alpha_q1	alpha_q3	Rosetta n	n_q1	n_q3	Rosetta th_r	th_r_std	Rosetta th_s	th_s_std	log(alpha)	log(alpha)_std	log(n)	log(n)_std	Ks	Ks_std	Ko	Ko_std	L	L_std
Perry	Duco-Pahrange-Lemm association	1522	very stony sandy loam	S_Loam	0.02666859	0.00734514	0.09682779	1.44877185	1.12460497	1.86637969	0.039	0.054	0.387	0.085	-1.574	0.56	0.161	0.11	379.92	158.4	285.6	50.4	-0.861	-0.73

Perry		Farad		Carr		Walker	
Unburned mean		Unburned mean		Unburned mean		Unburned mean	
u alpha	0.03909048	u alpha	0.01875	u alpha	0.06675	u alpha	0.02495
u n	1.43909524	u n	1.3485	u n	1.4575	u n	1.7105
u thr	0.05886122	u thr	0.06678916	u thr	0.03933735	u thr	0.0115
u ths	0.35703908	u ths	0.48670683	u ths	0.53696787	u ths	0.5315
Burned		Burned		Burned		Burned	
alpha mean	0.0510588	alpha mean	0.05212	alpha mean	0.11777692	alpha mean	0.0238275
alpha min	0.00286	alpha min	0.0163	alpha min	0.0102	alpha min	0.00861
alpha max	0.1736	alpha max	0.1178	alpha max	0.5	alpha max	0.0343
n mean	1.67216	n mean	1.3584	n mean	1.47376923	n mean	1.64925
n min	1.262	n min	1.311	n min	1.235	n min	1.53
n max	3.584	n max	1.444	n max	1.716	n max	1.867
Thr mean	0.05050197	Thr mean	0.08130924	Thr mean	0.02525178	Thr mean	0.009
Thr min	0.02080321	Thr min	0.02987952	Thr min	0.00445783	Thr min	0.004
Thr max	0.14989034	Thr max	0.12188755	Thr max	0.0997992	Thr max	0.014
Ths mean	0.44336301	Ths mean	0.54041767	Ths mean	0.45878591	Ths mean	0.452
Ths min	0.27084337	Ths min	0.48277108	Ths min	0.32827309	Ths min	0.286
Ths max	0.63089435	Ths max	0.65903615	Ths max	0.6148996	Ths max	0.522

Dolan		Dixie		Taboose	
Unburned mean		Unburned mean		Unburned mean	
u alpha	0.12343333	u alpha	0.0255	u alpha	0.0748
u n	1.23366667	u n	1.518	u n	1.438
u thr	0.0087	u thr	0.01725	u thr	0.009
u ths	0.55233333	u ths	0.547	u ths	0.4325
Burned		Burned		Burned	
alpha mean	0.07465	alpha mean	0.03735	alpha mean	0.0726
alpha min	0.0269	alpha min	0.0273	alpha min	0.0662
alpha max	0.1486	alpha max	0.0474	alpha max	0.079
n mean	1.385	n mean	1.4445	n mean	1.7635
n min	1.244	n min	1.3	n min	1.612
n max	1.487	n max	1.589	n max	1.915
Thr mean	0.02266667	Thr mean	0.01	Thr mean	0.0075
Thr min	0.01	Thr min	0.005	Thr min	0.007
Thr max	0.033	Thr max	0.015	Thr max	0.008
Ths mean	0.55033333	Ths mean	0.578	Ths mean	0.395
Ths min	0.451	Ths min	0.5	Ths min	0.389
Ths max	0.615	Ths max	0.656	Ths max	0.401

Table S3. Mean unburned values, burned mean, minimum and maximum values of Van Genuchten parameters for all fires

Figures S2-S8. (Pages 43-49) Fire-specific plots of HYDRUS simulations at 40 mm/hr rainfall intensity

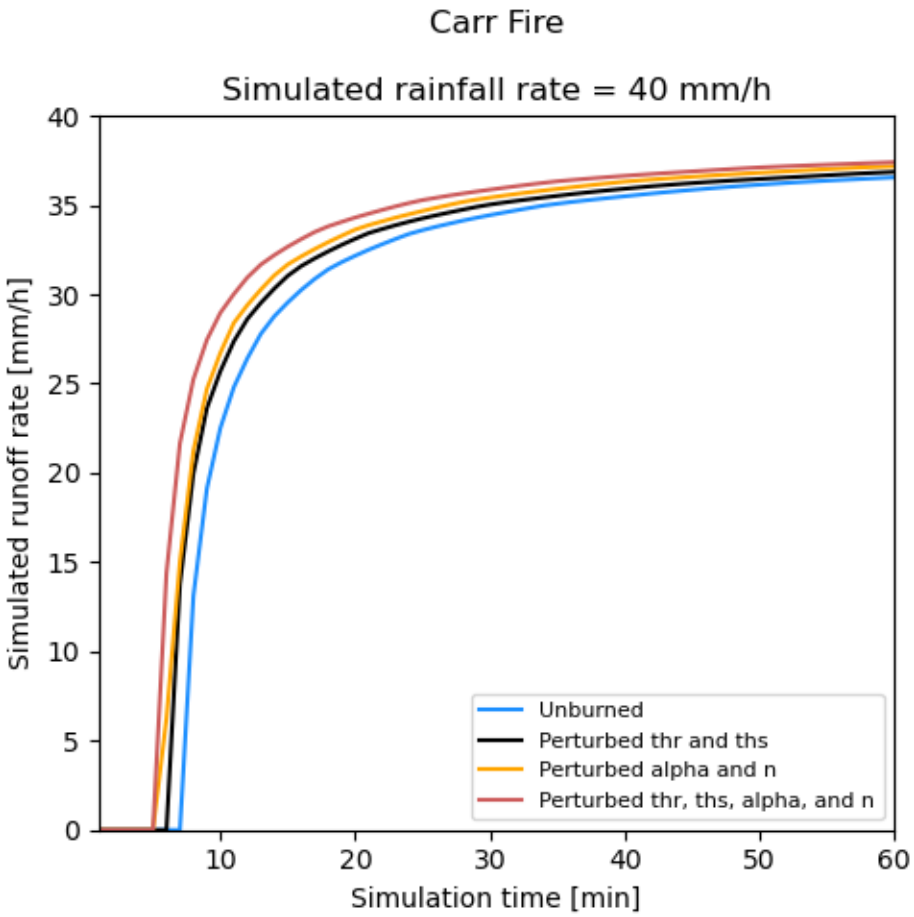

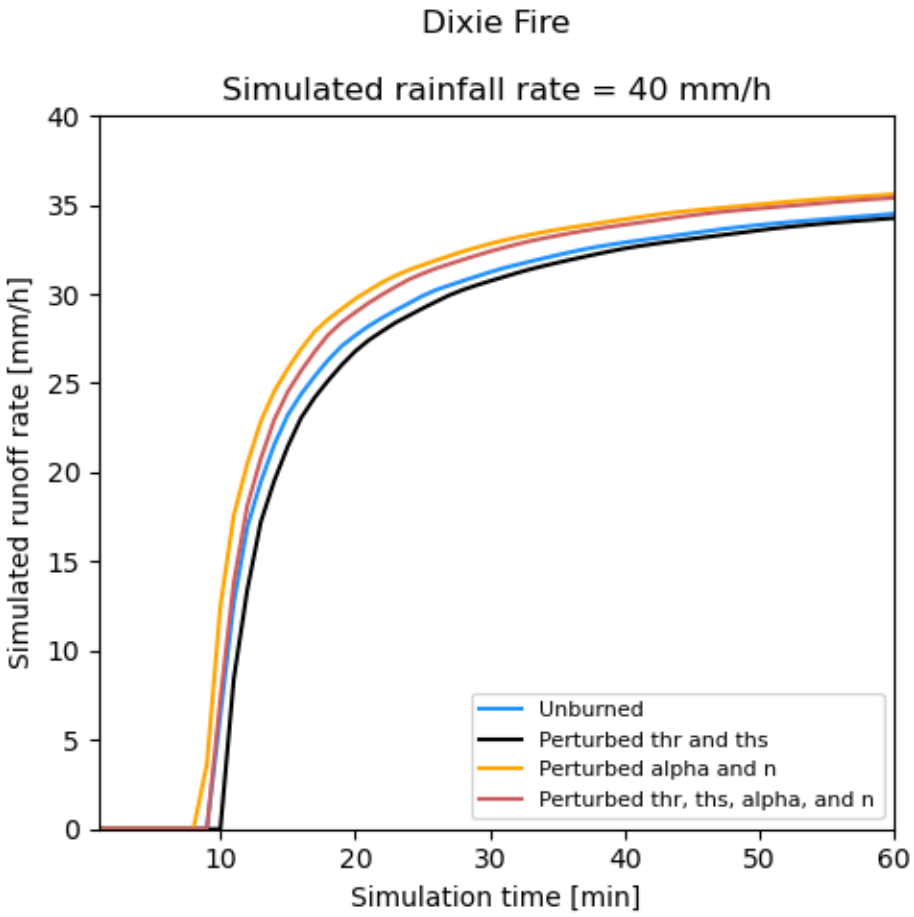
Dixie Fire
Simulated rainfall rate = 40 mm/h
Simulated runoff rate [mm/h]
Simulation time [min]
0
5
10
15
20
25
30
35
40
10
20
30
40
50
60
Unburned
Perturbed thr and ths
Perturbed alpha and n
Perturbed thr, ths, alpha, and n

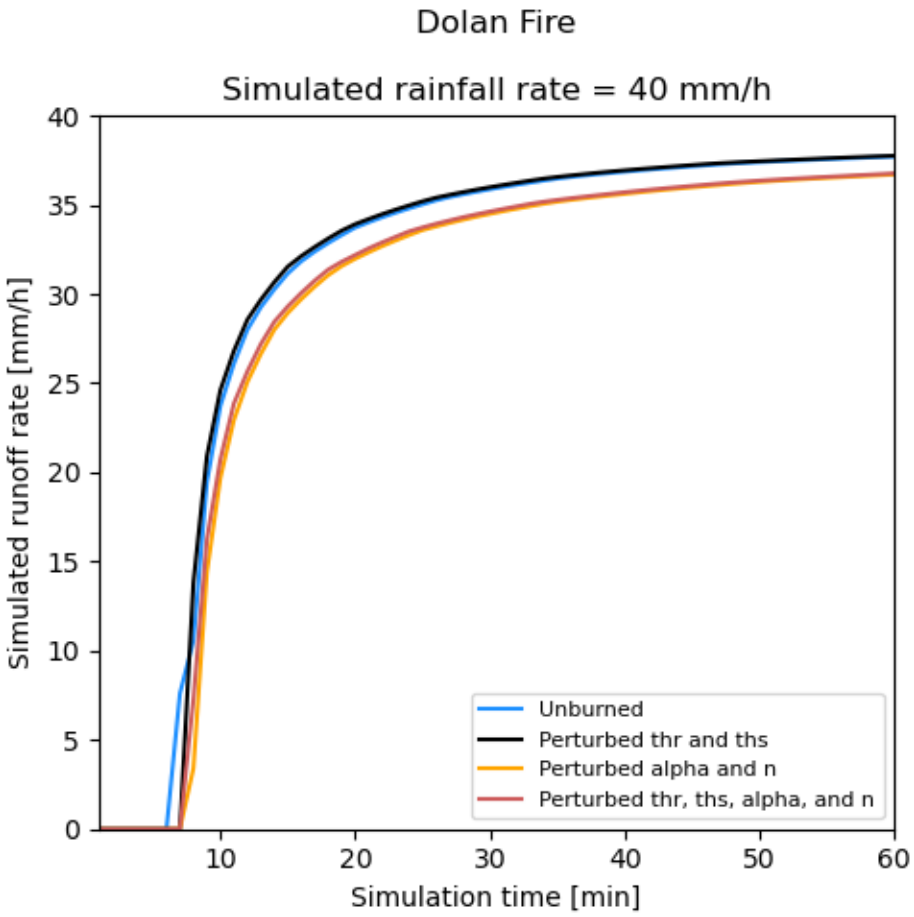
Dolan Fire
Simulated rainfall rate = 40 mm/h
Simulated runoff rate [mm/h]
Simulation time [min]
0
5
10
15
20
25
30
35
40
10
20
30
40
50
60
Unburned
Perturbed thr and ths
Perturbed alpha and n
Perturbed thr, ths, alpha, and n

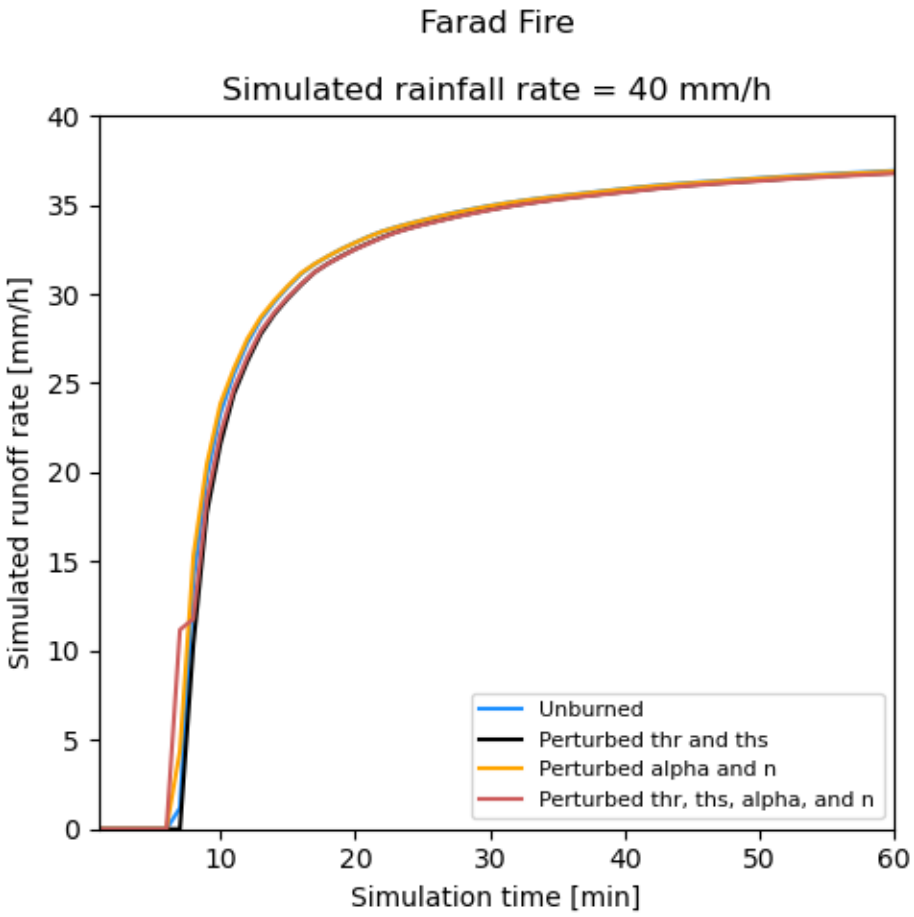
Farad Fire
Simulated rainfall rate = 40 mm/h
Simulated runoff rate [mm/h]
Simulation time [min]
0
5
10
15
20
25
30
35
40
10
20
30
40
50
60
Unburned
Perturbed thr and ths
Perturbed alpha and n
Perturbed thr, ths, alpha, and n

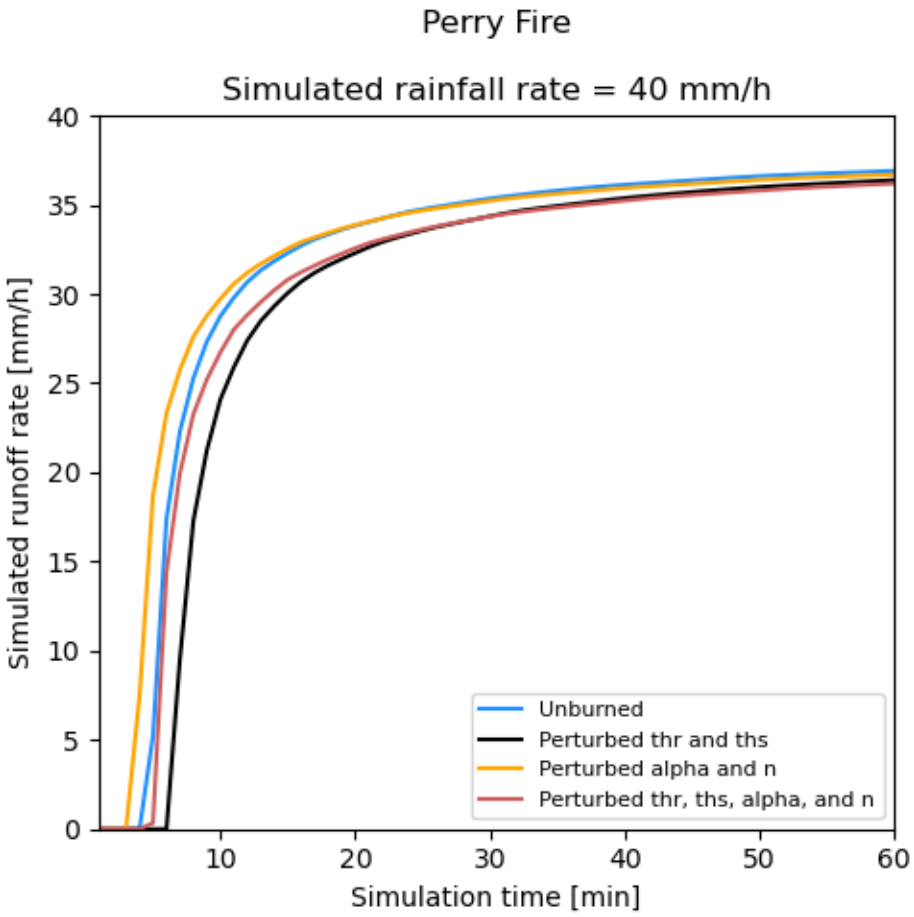
Perry Fire
Simulated rainfall rate = 40 mm/h
Simulated runoff rate [mm/h]
Simulation time [min]
0
5
10
15
20
25
30
35
40
10
20
30
40
50
60
Unburned
Perturbed thr and ths
Perturbed alpha and n
Perturbed thr, ths, alpha, and n

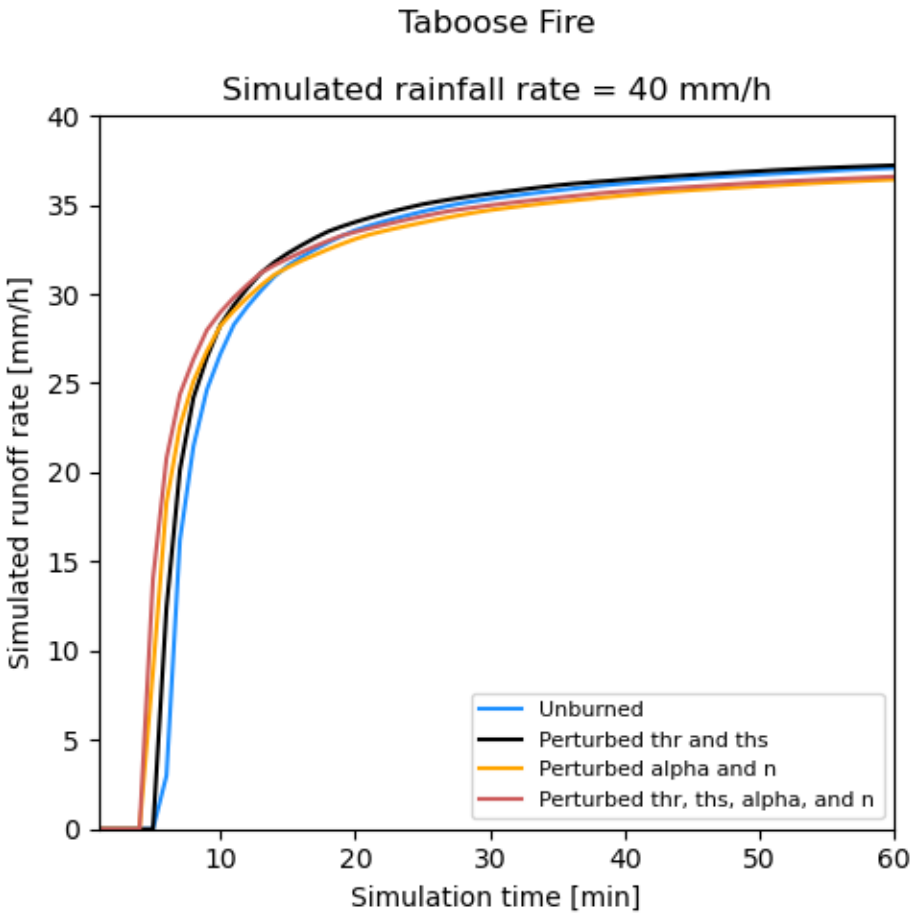
Taboose Fire
Simulated rainfall rate = 40 mm/h
Simulated runoff rate [mm/h]
Simulation time [min]
0
5
10
15
20
25
30
35
40
10
20
30
40
50
60
Unburned
Perturbed thr and ths
Perturbed alpha and n
Perturbed thr, ths, alpha, and n

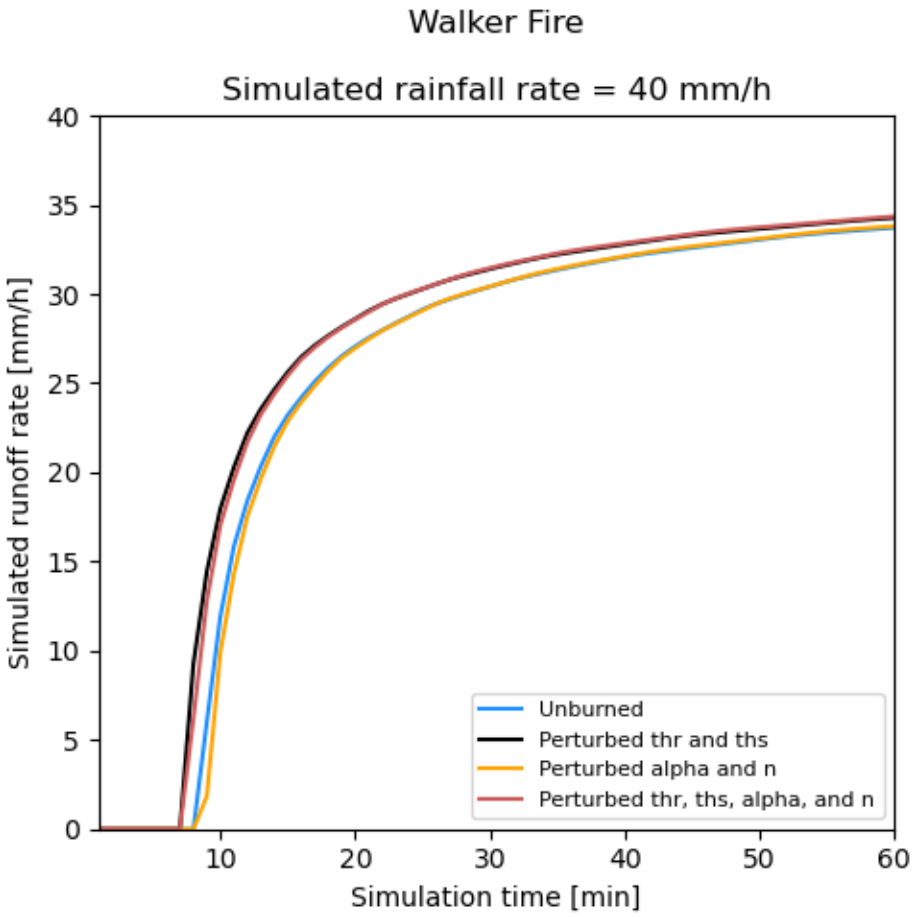
Walker Fire
Simulated rainfall rate = 40 mm/h
Simulated runoff rate [mm/h]
Simulation time [min]
0
5
10
15
20
25
30
35
40
10
20
30
40
50
60
Unburned
Perturbed thr and ths
Perturbed alpha and n
Perturbed thr, ths, alpha, and n

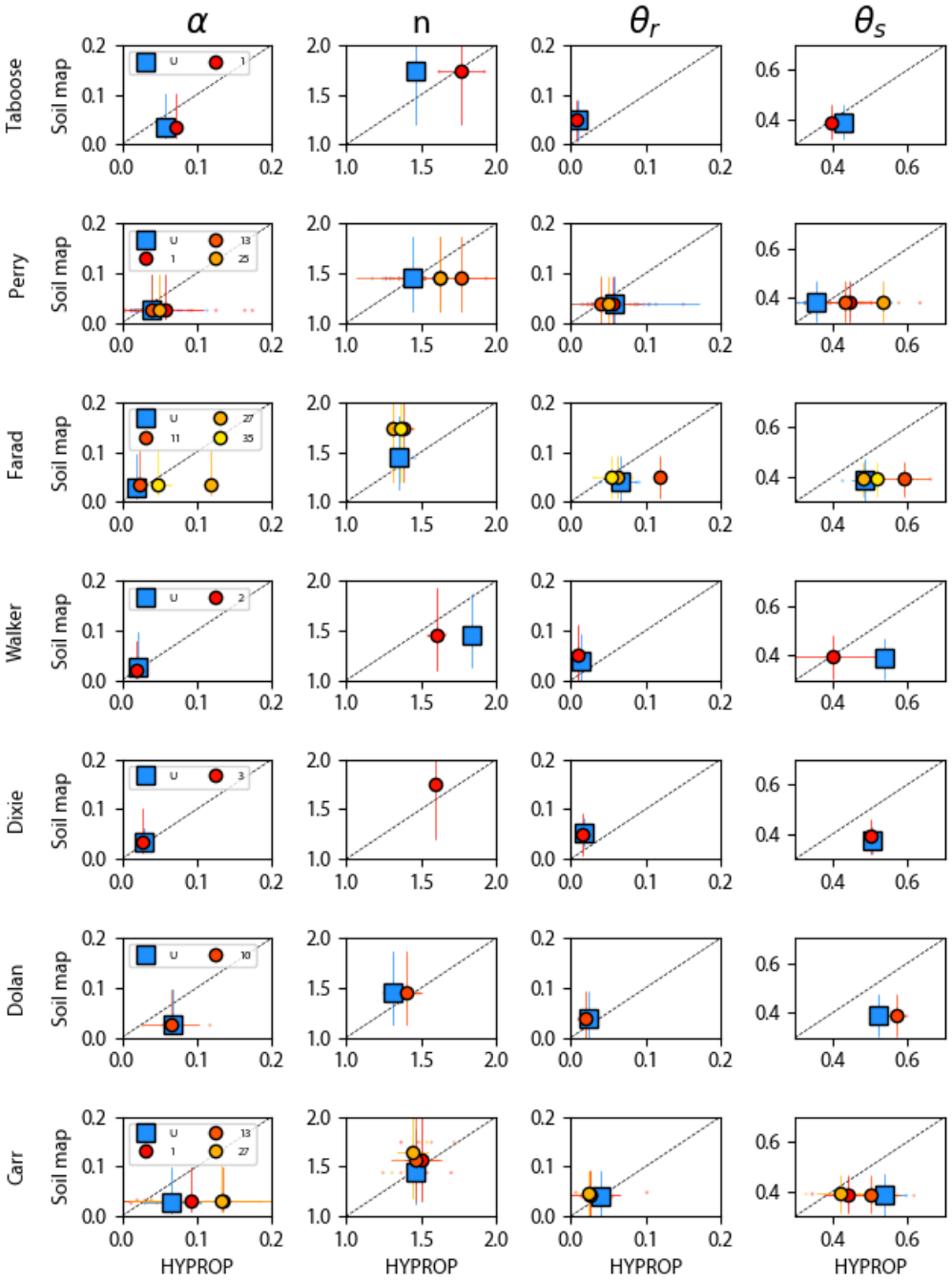

Figure S9. Comparison of measured unburned and burned Van Genuchten parameters (X axis) with the Rosetta database Van Genuchten parameters associated with mapped USDA soil textures (Y axis). Blue squares are unburned soils, red circles are the first measurements after the fire, orange circles are the second year post-fire and yellow circles are three years post-fire.